Trace element partitioning in strongly peraluminous rare-metal silicic magmas - Implications for fractionation processes and for the origin of the Macusani Volcanics (SE Peru)

Michel Pichavant, Saskia Erdmann, Daniel J Kontak, Julie Michaud, Arnaud Villaros

Journal Pre-proofs

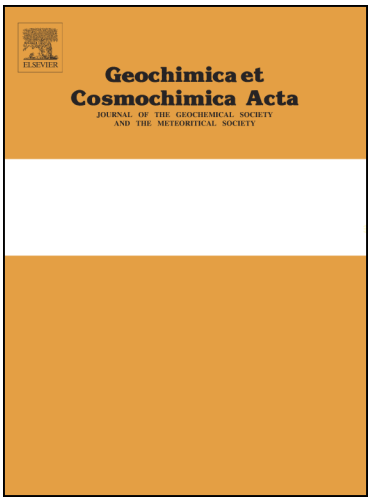

Trace element partitioning in strongly peraluminous rare-metal silicic magmas - Implications for fractionation processes and for the origin of the Macusani Volcanics (SE Peru)

Michel Pichavant, Saskia Erdmann, Daniel J. Kontak, Julie Michaud, Arnaud Villaros

PII: S0016-7037(23)00583-5
DOI: https://doi.org/10.1016/j.gca.2023.11.021
Reference: GCA 13235

To appear in: *Geochimica et Cosmochimica Acta*

Received Date: 3 May 2023
Accepted Date: 22 November 2023

Please cite this article as: Pichavant, M., Erdmann, S., Kontak, D.J., Michaud, J., Villaros, A., Trace element partitioning in strongly peraluminous rare-metal silicic magmas - Implications for fractionation processes and for the origin of the Macusani Volcanics (SE Peru), *Geochimica et Cosmochimica Acta* (2023), doi: https://doi.org/10.1016/j.gca.2023.11.021

Trace element partitioning in strongly peraluminous rare-metal silicic magmas - Implications for fractionation processes and for the origin of the Macusani Volcanics (SE Peru)

Michel Pichavant [a]*, Saskia Erdmann [a], Daniel J. Kontak [b]

Julie Michaud [c], Arnaud Villaros [a]

[a] Université d'Orléans, Institut des Sciences de la Terre d'Orléans (ISTO), UMR 7327, 1A rue de la Férollerie, CS 20066, 45071, Orléans Cedex 02, France

[b] Laurentian University, Harquail School of Earth Sciences, 935 Ramsey Lake Rd., Sudbury, Ontario, PC2E6, Canada

[c] Leibniz Universität Hannover, Institut für Mineralogie, Callinstr. 3, 30167 Hannover, Germany

*Corresponding author. *E-mail address*: michel.pichavant@cnrs-orleans.fr (M. Pichavant)

ABSTRACT

The Macusani Volcanics and related rocks (SE Peru) are well known examples of erupted strongly peraluminous rare-metal rich silicic magmas. We used the phenocryst/matrix glass method to determine relevant mineral/melt partition coefficients to facilitate modeling of such systems. Concentrations of trace (Li, Be, B, Al, P, Ti, Mn, Zn, Ge, Rb, Sr, Zr, Nb, Sn, Cs, Ba, La, Sm, Eu, Gd, Yb, Ta, W, Pb and U) and major elements were measured in obsidians, matrix glasses, glass inclusions, phenocrysts and phases from biotite reaction zones by Laser-Ablation ICP-MS and Electron Microprobe Analysis. The derived phenocryst/melt partition coefficients for quartz, plagioclase, sanidine, biotite, muscovite, andalusite and ilmenite are compared with values from reference silicic magmas and literature. Mineral/biotite partition coefficients are calculated for tourmaline and hercynite. The database is then applied to model chemical fractionation in Macusani magmas. Fractional crystallization and partial melting trends (with the B concentration used as a proxy for the fraction of residual liquid) generate progressively more evolved (higher Rb, Nb, Sn, Cs and Ta and lower Sr, Ba and Pb) residual liquids. The trace element concentrations in obsidians are reproduced for 50-70% crystallization of matrix glasses from ash-flow tuffs. This demonstrates that differentiation of magmas parental to the ash-flow tuffs can generate the highly evolved obsidian-forming liquids. Based on this, we

present an updated model for crustal melting and the generation of the Macusani magmas. A metapelitic component dominates the source region but calcic plagioclase cores enriched in Sr, Ba and La suggest an affiliation with mafic magmas, which were likely potassic to ultrapotassic. The presence of a mafic component is consistent with the high heat fluxes in the source region and accounts for specific magmatic variables (i.e., middle crustal anatectic zone, very reducing fO_2, high F). Petrogenetic processes differ significantly between Macusani Volcanics suites and two-mica leucogranites despite both having nearly identical source rocks, mineral assemblages and compositions.

Keywords: Peraluminous silicic magmas, trace elements, partition coefficients, chemical fractionation, crustal melting

1. Introduction

The critical metals Sn, W, Nb and Ta, together with other lithophile (Be, Cs, Rb, U) and fluxing (Li, B, F, P) elements can be strongly concentrated in silicic volcanics (Kovalenko and Kovalenko, 1976; Christiansen et al., 1984; Pichavant et al., 1987), rare-metal granites (Cuney et al., 1992; Raimbault et al., 1995; Breiter et al., 1997; Michaud et al., 2020) and rare element pegmatites (Roda-Robles et al., 2018; Villaros et al., 2019; Ballouard et al., 2020). These geochemically enriched igneous rocks constitute primary resources for critical metals such as Li, Be, Nb, Ta, Cs (Partington et al., 1995; Stilling et al., 2006). Remobilization of magmatic concentrations leads to the formation of secondary hydrothermal deposits of Sn, W and other metals (Stemprok, 2016; Korges et al., 2018). Although rare-metal silicic magmas are of different types (Linnen and Cuney, 2005; Romer and Pichavant, 2021), models for their generation divide into two groups: (1) differentiation from less evolved parental magmas (e.g., Raimbault et al., 1995; Cerny et al., 2005; London, 2008; Hulsbosch, 2019); and (2) direct anatectic origin (e.g., Stewart, 1978; Christiansen et al., 1986; Nabelek et al., 1992a; b; Cuney and Barbey, 2014; Müller et al., 2017; Michaud et al., 2021). One way to distinguish between these two models is through geochemical modelling but this approach is presently hampered by several limitations. First, no partitioning dataset covers the whole range of elements, mineral phases, melt compositions and magmatic conditions relevant to rare-metal silicic magmas (Villaros and Pichavant, 2019). Second, the behavior of elements such as P, Mn, Sn, Nb, Ta, Zr, Hf is often governed by saturation of accessory phases (apatite, amblygonite-montebrasite, cassiterite, columbite-tantalite, zircon) in the melt (Michaud and Pichavant, 2020) which requires that their solubilities are known for flux-rich melts (Linnen, 1998).

To overcome these limitations, we present in this study mineral/melt partition coefficients for 25 pertinent elements and phases and for conditions typical of strongly peraluminous rare-metal silicic magmas. Partition coefficients have been classically derived from element concentrations in phenocrysts and glasses coexisting at equilibrium (e.g., Nash and Crecraft, 1985), the main alternative method being experimental determinations as reviewed by Nielsen et al. (2017). Lithium, Be, Sr, Rb, Cs, Ba and F mineral/melt partition coefficients have been experimentally determined for peraluminous magmas (Icenhower and London, 1995; 1996, 1997; Evensen and London, 2002; Pichavant et al., 2016; Pichavant, 2022; see Villaros and Pichavant, 2019 for a summary). However, the experimental approach is faced

with a number of difficulties, one being the small size of mineral phases (e.g., Pichavant, 2022), and experimentally determined partition coefficients are still lacking for many elements, in particular the critical metals (Sn, W, Nb, Ta). In comparison, a large phenocryst/glass partitioning database is available for rhyolites, including highly fractionated magmas such as topaz rhyolites (e.g., Congdon and Nash, 1991; Dailey et al., 2018) and less fractionated magmas (Bachmann et al., 2005; Padilla and Gualda, 2016 and references therein). However, these data are generally not directly applicable to rare-metal granites which have different bulk compositions and phase assemblages. Rare-metal granites and pegmatites from the Variscan and Himalayan belts are both strongly peraluminous and P-rich (PHP types, Linnen and Cuney, 2005; see also Raimbault et al., 1995; Roda-Robles et al., 2018; Liu et al., 2020; Michaud et al., 2020). They crystallize a specific magmatic assemblage including muscovite, andalusite, tourmaline, garnet, cordierite, hercynite, Al-rich biotite and also ilmenite instead of magnetite (e.g., Clarke, 1981). Glass is absent or preserved only as glass inclusions (Thomas and Davidson, 2012). Their extrusive equivalents, although rare, include the Macusani Volcanics from SE Peru (Pichavant et al., 1988a; b) and the Richemont rhyolite (Massif Central, France, Raimbault and Burnol, 1998), both offering great potential for the determination of partition coefficients with the phenocryst/glass approach. In this paper, trace element data on the Macusani Volcanics suite are presented and a set of partition coefficients applicable to strongly peraluminous rare-metal silicic magmas is constructed.

The Macusani Volcanics (SE Peru), have attracted considerable interest since the 1980s. They are mainly exposed as ash-flow tuffs (Noble et al., 1984), obsidians being present in minor amounts (Pichavant et al., 1987 and references therein). These obsidians (macusanites) have been considered as a reference composition for pegmatitic liquids (London, 2015) and have become used as a geochemical standard both for terrestrial and extraterrestrial applications (Fabre et al., 2011). However, their origin is still unclear since parental magmas have remained elusive. The Macusani Volcanics are also reference examples for strongly peraluminous felsic extrusive silicic magmas (Frost et al., 2016) and their origin by partial melting of the continental crust has been demonstrated (Pichavant et al., 1988a, b). However, the exact nature of source rocks is still uncertain and mechanisms of partial melting in the anatectic region, where mafic melts have been postulated to serve as heat sources (Pichavant et al., 1988a; b; Cheilletz et al., 1992), are yet to be clarified.

In this paper, we report new major and trace element analyses of coexisting minerals and glasses from the Macusani Volcanics. Element concentrations and distributions between phases are documented for 24 trace elements and from this an internally consistent set of partition coefficients is presented. Additionally, these new trace element data are used to: (1) discuss fractionation processes in peraluminous silicic magmas and (2) update the genetic model proposed for the Macusani Volcanics (Pichavant et al., 1988a, b).

2. The Macusani Volcanics

2.1. Regional and local geological setting

The Macusani Volcanics are located in the Puno Department, southeastern Peru, ~50 km north of Lake Titicaca. The area belongs to the Cordillera de Carabaya segment of the Central Andean Eastern Cordillera (Cordillera Oriental). This region exposes a diverse assemblage of Oligocene to Miocene (the Picotani Group, 22-26 Ma) and Miocene to Pliocene (the Quenamari Group, ~4-17 Ma) volcanic and hypabyssal intrusive rocks (Laubacher, 1978; 1988; Sandeman et al., 1996; 1997; Sandeman and Clark, 2004). The Quenamari Group formations outcrop mainly in the Quenamari and Picotani fields and in a few other smaller locations (Sandeman et al., 1997).

The geology of the Quenamari field has been described previously (Laubacher, 1978; Noble et al., 1984; Pichavant et al., 1987; 1988a and references therein; Cheilletz et al., 1992; Sandeman et al., 1997). More recently, field relations and ages have been summarized by Li (2016). The field comprises volcanic rocks ("Macusani Volcanics") which cover an area of 860 km^2 at an average altitude of ~4400 m, plus a few hypabyssal plutonic rocks. The volcanic rocks form a flat-lying sequence of relatively uniform, massive, whitish-grey rhyolitic ash-flow tuffs. The maximum thickness of the sequence is 500 m and their estimated volume is 430 km^3 (Cheilletz et al., 1992; Li, 2016). The volcanic rocks unconformably overlie deformed Paleozoic sedimentary strata, Jurassic peralkaline volcanic rocks and Oligocene to Miocene volcanic rocks from the Picotani Group. The ash-flow tuffs locally contain pumice clasts, microgranite and rhyolite enclaves and country rock xenoliths (limestones, pelites, quartzites). The obsidians (i.e., macusanites) are mainly found as pebbles in stream gravels or more rarely as small inclusions in the tuffs (Pichavant et al., 1987). Two major eruptive cycles at 10±1 Ma and 7±1 Ma have been recognized from $^{40}Ar/^{39}Ar$ data (Cheilletz et al., 1992). Obsidians have younger ages (as young as ~4 Ma, Pichavant et al., 1987 and references therein; Poupeau et al., 1992; 1993) and so volcanic activity in the Quenamari field extended to < 7 Ma. In the Picotani field, the Quenamari Group volcanic rocks are older than in the Quenamari field (16-17 Ma, Pichavant et al., 1988a; Sandeman et al., 1997). They comprise two main stratigraphic units covering a total areal extent of 160 km^2 and a thickness of 200 m corresponding to a magma volume of 32 km^3 minimum (Sandeman et al., 1997). The rhyolitic flows unconformably overlie the basement sedimentary formations and volcanic rocks from the Picotani Group (Sandeman et al., 1997). Lithic fragments include rhyolite and country rock xenoliths (slate, sandstone and rare limestone, Sandeman et al., 1997).

The mineralogy of Quenamari Group volcanic rocks is exceptional, being typical of strongly peraluminous granites and highly unusual for rhyolites. In the Quenamari field, the crystal-rich (40-55 vol.%) ash-flow tuffs contain quartz, sanidine, plagioclase, biotite, muscovite, andalusite, cordierite, tourmaline, apatite and ilmenite phenocrysts (Pichavant et al., 1988a; Li, 2016). The matrix is fine-grained and mostly recrystallized to clay minerals. The crystal-poor obsidians contain a microphenocryst assemblage that is nearly identical to the phenocryst assemblage in the tuffs (Pichavant et al., 1988a). In the Picotani field (Sandeman et al., 1997), phenocrysts are more abundant (up to 70 vol%) and coarser than in the Quenamari field. Another difference concerns the matrix which, in the Picotani rocks, can be totally glassy and unaltered. Quartz, sanidine, plagioclase, biotite, muscovite and apatite are the main phenocrysts (Sandeman et al., 1997).

Most geochemical data on Quenamari Group volcanic rocks are for the Quenamari field and only a few major element analyses are available for the other volcanic fields (Noble et al., 1984; Laubacher et al., 1988; Pichavant et al., 1988b; Sandeman and Clark, 2004). Whole-rock compositions are all very similar, rhyolitic, strongly peraluminous (A/CNK > 1.2, normative corundum > 2%) and felsic (high Na_2O, K_2O and low FeO_t, MgO, CaO, TiO_2). Concentrations of fluxing elements (P_2O_5, F, Li_2O and B_2O_3) are up to the 1 wt% level in obsidians. Trace

element patterns are characterized by high lithophile (Be, Rb, Cs) and rare-metal (Sn, W, Nb, Ta, U) concentrations and low Ba, Sr, Eu, Th. The Sr-O-Pb-Nd isotopic data are consistent with an origin for the Macusani Volcanics by partial melting of upper crustal dominantly pelitic source rocks (Pichavant et al., 1987; 1988b).

2.2. Sample selection

Most Quenamari field ash-flow tuffs do not preserve fresh matrix glass and the size of microphenocrysts in obsidians (< 10 μm except andalusite, Pichavant et al., 1988a) makes their trace element analysis difficult. Thus, our investigations concentrated on a few ash-flow tuffs with matrix glasses amenable to trace element analysis. Three samples from the Quenamari field were selected. They contain numerous pumice clasts with fresh glass and also glass inclusions in phenocrysts (MIs). They come from basal contacts and lower levels of the volcanic sequence in the Huiquiza area, in the eastern part of the Quenamari field (see maps in Pichavant et al., 1988a; Cheilletz et al., 1992). Sample MH1 was previously included in mineralogical and geochemical studies on Macusani ash-flow tuffs (Pichavant et al., 1988a; b) whereas the two others (MA85-4, MA85-7) are new samples, having been collected by the first author in 1985. In the Picotani field, the Quenamari Group rhyolitic flows are characterized by high proportions of unaltered glass as lapilli and groundmass (Sandeman et al., 1997). Two samples (CR85-1, CR85-2), also collected by the first author in 1985, were selected. They come from the southern shore of Rio Carabaya near Hacienda Huacchane (see map in Sandeman et al., 1997). These samples also contain MIs.

Among these five ash-flow tuffs (designated as “glass-bearing samples” below), the three Quenamari samples do not exhibit all mineral assemblages and textures characteristic of the Macusani Volcanics (Pichavant et al., 1988a). Therefore, additional Quenamari samples (designated as “glass-free samples” below) were included in the analytical program. These served to more completely analyse muscovite, andalusite, tourmaline and hercynitic spinel, to investigate specific textures (biotite melting reactions, plagioclase cores), check the representativity of mineral compositions and complement the trace element data obtained on the glass-bearing samples. Six ash-flow tuffs from the Huiquiza section (MH2, -3, -4, -6, -7, -8), previously subjected to detailed mineralogical and geochemical investigations (Pichavant et al., 1988a), and three from the Chapi area in the NW part of the Quenamari field (CHA2, CHA85-10, CHA85-11), were investigated. Sample CHA2 has been studied previously (Pichavant et al., 1988a) whereas both samples CHA85-10 and CHA85-11 are new, having been collected by the first author in 1985.

Several previously investigated obsidians (JV1, JV2, JV3, CH0) from the Quenamari field (Pichavant et al., 1987) were re-analyzed mainly for internal consistency with the matrix glasses and MIs analyzed in the glass-bearing samples.

3. Analytical techniques

3.1. Sample characterization

Thin sections of both conventional (30 µm) and oversize (80 µm) thicknesses were prepared and examined by optical microscopy. Selected areas were studied by scanning electron microscopy (SEM) to (1) document textures and sizes of matrix glass domains and check for microlites, (2) locate and examine glass inclusions exposed at the surface of phenocrysts, (3) determine mutual relations between mineral phases (e.g., inclusion relationships) and (4) image zonation in phenocrysts. A Zeiss Merlin Compact (ISTO, Orléans) instrument operating under either secondary or back-scattered electron (BSE) mode and fitted with a Bruker energy dispersive system (EDS) was used for investigating glass and mineral textures. Zonations in quartz and sanidine were studied with a MIRA 3 Tescan scanning electron microscope (BRGM, Orléans) equipped with a cathodoluminescence (CL) detector and operated under 15 kV acceleration voltage.

3.2. Major element analysis

Glasses and minerals were analyzed by electron microprobe (EMPA) using a Cameca SX Five instrument (ISTO, Orléans). Silicate phases were analyzed in punctual mode for SiO_2, TiO_2, Al_2O_3, FeO, MnO, MgO, ZnO, CaO, Na_2O, K_2O, P_2O_5 and F under 15 kV acceleration voltage, 6 nA sample current and 10 and 5 s counting times on peak and background respectively. Although these conditions also served for a few oxides, most ilmenites and hercynitic spinels were analyzed for TiO_2, Al_2O_3, FeO, MnO, NiO, MgO, ZnO, SnO_2, WO_3, Nb_2O_5 and Ta_2O_5 under 20 kV acceleration voltage and 20 nA sample current. Standards were natural silicates and oxides. For the analysis of glasses, the beam size (usually 1-2 µm) was defocused to 10 µm and the data were checked against previous results on obsidians JV2, JV3 and CH0 (Pichavant et al., 1987). Alkali migration was not corrected for and thus it is likely that the reported glass Na_2O and K_2O contents are slightly underestimated. We checked that alkali migration was effectively minimized (if not totally suppressed) by comparing data with a 10 µm beam with results using smaller and larger beam sizes (1 and 20 µm). Relative analytical errors on glasses, determined from multiple analyses of obsidian JV2, are: 0.5–1% (SiO_2), 80% (TiO_2), 1-1.5% (Al_2O_3), 25% (FeO_t), 100% (MnO, MgO, ZnO), CaO (15%), 5-10% (Na_2O, K_2O, F), P_2O_5 (20%). For minerals, analytical errors are 1% relative for SiO_2 and Al_2O_3, 2% for CaO, 3% for FeO, MgO, ZnO and TiO_2, 5% for MnO, Na_2O and K_2O, 10 % for F, NiO, SnO_2, WO_3, Nb_2O_5 and Ta_2O_5. The quality of the new EMPA data was also checked by comparison with previous results (Pichavant et al., 1988a). A few Na, K, Ca X-ray distribution maps and electron microprobe traverses were also acquired on selected feldspar phenocrysts.

3.3. Trace element analysis

Trace element concentrations in glasses and mineral phases were determined by laser ablation inductively coupled plasma mass spectrometry (LA ICP-MS). Two different instruments were successively used. The early analyses were performed with a RESOlution

ArF excimer laser (λ = 193 nm) coupled to a Thermo Finnigan Element XR ICP-MS at the IRAMAT-ISTO-CEMHTI facility (Orléans). More recently, a RESOlution -SE 193 nm excimer laser coupled to an Agilent 8900 QQQ ICP-MS was used at the ISTO facility (Orléans). For glasses and silicate minerals, SiO_2 was used as an internal standard, TiO_2 for ilmenites and Al_2O_3 for hercynitic spinels. Spatial correspondence between the major and trace element data was established from EMPA analyses obtained near the LA ICP-MS pits. NIST610 was used as an external standard for silicate mineral and glass analyses (with reference values of Pearce et al. 1997) whereas GSE-2G was used as an external standard for the ilmenite analyses (with USGS reference values). Glasses BCR-2G (GeoRem database, Jochum et al., 2005) and obsidians JV2 and CH0 (Pichavant et al. 1987) were used as quality control. These reference glasses were analyzed approximately three times at the beginning and at the end of each run of ten analyses. Over the data acquisition period (2018-2022), the laser ablation parameters were varied and slightly adjusted. For obsidians and matrix glasses, frequency was set at 5 or 10 Hz, fluence at 2.5 or 5 J.cm^{-2}, and various beam sizes, from 10 to 100 µm, were tested. Quartz, feldspars and other silicate minerals were ablated using a frequency of either 5 or 10 Hz, a fluence of 7, 5 or 4 J.cm^{-2} respectively and a beam diameter generally of either 30 or 64 µm. Oxides were analyzed with a 10 Hz frequency and a 7 J.cm^{-2} fluence with a beam diameter of 10 µm. Glass inclusions were ablated with a lower frequency (3 Hz) and using a SQUID to homogenize the signal. A total of 28 isotopes (^{7}Li, ^{9}Be, ^{11}B, ^{23}Na, ^{27}Al, ^{29}Si, ^{31}P, ^{39}K, ^{49}Ti, ^{55}Mn, ^{66}Zn, ^{72}Ge, ^{85}Rb, ^{88}Sr, ^{90}Zr, ^{93}Nb, ^{118}Sn, ^{133}Cs, ^{137}Ba, ^{139}La, ^{147}Sm, ^{153}Eu, ^{157}Gd, ^{172}Yb, ^{181}Ta, ^{182}W, ^{208}Pb, ^{238}U) were measured. The isotopes were selected such that isobaric and matrix-dependent polyatomic interferences did not play a significant role with the possible exception of ^{66}Zn and ^{72}Ge (May and Wiedmeyer 1998; Thomas, 2013; Jenner and Arevalo 2016). For Zn, polyatomic interference by $^{50}Ti^{16}O^{+}$ may have played a role (mostly for ilmenite) and, for Ge, polyatomic interferences of $^{56}Fe^{16}O^{+}$ and $^{40}Ca^{16}O_2^{+}$ may have caused interference (for most analyzed phases except quartz), but instruments were tuned to low oxide production rate to mitigate the issue. On the basis of published Zn and Ge compositions and our quality control values as well as the determined partition coefficients (see below), the reported values are considered accurate (and interferences insignificant).

The raw data were processed off-line using the Glitter software (Griffin, 2008) where time-resolved signals were examined one by one. Element concentrations were calculated for the initial ~ 30 s of all ablation signals relative to the gas blank (~ 20 s), with a linear interpolation across standard analyses. The LA ICP-MS data were carefully checked first on the basis of the concentrations of major elements (Na, Al, Si and K which were measured together with the trace elements although not reported) to confirm the nature of the phase analyzed and verify consistency. Subsequent to this, all time-resolved spectra were screened for contamination by inclusions or mixed phase analysis (narrow spikes or otherwise irregular spectra). Spectra with narrow spikes at the beginning or end were filtered to remove these spikes and then accepted, if the extracted compositions were within standard deviation of other compositional data. Overall irregular spectra or spectra with multiple spikes were discarded. The LA ICP-MS data for glasses were averaged and standard deviations, relative standard deviations and average analytical errors (1 σ, calculated with Glitter) are reported. For phenocrysts, individual analyses are given and also individual analytical errors (1 σ, calculated with Glitter) since they vary with the concentration.

4. Results

4.1. Phase assemblages and textures

The three glass-bearing Quenamari (Macusani hereafter) ash-flow tuffs contain numerous highly vesicular pumice clasts of various shapes and sizes (i.e., from 0.3 up to 2 mm), which commonly host a few phenocrysts (Fig. 1a). Glass in pumice clasts forms small (< 50 μm wide) elongated filaments devoid of microlites and separated from each other by stretched vesicles (Fig. 1b). The Picotani sample CR85-1 is very crystal-rich (~50% phenocrysts) and coarse-grained with phenocryst sizes mostly in the 0.5-3 mm range. The groundmass is almost entirely glassy with dense bubble-free zones passing progressively to more bubbly areas. Microlites are absent (Fig. 1c). CR85-2 is less crystal-rich and more fine-grained than CR85-1. Yet, the groundmass consists of large bubble-poor to bubble-rich microlite-free dense glassy areas, and is thus similar to in CR85-1.

In Macusani samples, phenocrysts are mostly from 0.1 up to 0.5 mm in size, but sometimes larger, and are usually broken and anhedral and more rarely euhedral (Fig. 1a). They commonly host inclusions of other mineral phases (see Pichavant et al., 1988a). MIs (Fig. 1d), are found exposed at the surface of mainly quartz and sanidine and less frequently of biotite phenocrysts. In the three glass-bearing samples, quartz (Qz), plagioclase (Pl), sanidine (Af), biotite (Biot), apatite (Ap) and ilmenite (Ilm) are the main phenocrysts. Muscovite (Mu) and andalusite (And, identification confirmed by Raman spectroscopy) are also phenocrysts in MH1 and in several glass-free samples (Pichavant et al., 1988a). Both phases are absent in MA85-4 and MA85-7 although an Al-silicate microphenocryst, most probably sillimanite (Sill), is present in MA85-4. Tourmaline (Tur) occurs as an inclusion in a MH1 Pl and as an isolated phenocryst in several glass-free samples (Pichavant et al., 1988a). Cordierite (Cd) is absent from the glass-bearing but can be common in some glass-free samples (Pichavant et al., 1988a). Hercynitic spinels (Hc) are systematic in biotite melting reaction zones (textures described in Pichavant et al., 1988a, see also below). Inclusions in major phases comprise Sill, zircon (Zrc), monazite (Mz) and Ilm. The two Picotani samples are mineralogically simpler. Both contain the same phenocryst assemblage (Qz, Pl, Af, Biot, Mu, Ap). Sill (identification confirmed by Raman spectroscopy), Zrc and Mz are included in major phenocrysts. Ilm was found only as inclusions in biotite. MIs occur exposed at the surface of Qz, Af and Biot phenocrysts. No And, Cd, Tur and Hc were found in the two Picotani samples studied.

4.2. Major element compositions of glasses

Glass filaments in pumice clasts (Macusani samples) and groundmass glasses (Picotani samples, collectively designated "matrix glasses" below) all have chemically homogeneous major element compositions (Table 1). For example, standard deviations calculated on the 20 analyses available for MH1 matrix glass are equal to or lower than instrumental errors. The electron microprobe data sum to low totals (96-97 wt%, Table 1) which suggests the presence of dissolved H_2O at concentrations of ~2 wt%. Matrix glasses are moderately silica-rich (~71-72 wt% SiO_2, n.b., data in Table 1 are not normalized to 100 % anhydrous), strongly peraluminous (A/CNK = 1.20-1.33; A' = 1000*(Al-(Na+K+2Ca)) at. = 46-71, normative corundum = 2.5-3.8%) and felsic (B' = 1000*(Fe+Mg+Ti) at. < 15, normative anorthite = 1.1-2.0%, Table 1). The F (0.20-0.60 wt%) and P_2O_5 (0.29-0.46 wt%) concentrations are

moderately high. Only small differences in matrix glass compositions appear between samples, i.e., the Macusani are slightly richer in normative Qz, and An and poorer in normative Ab than the Picotani glasses (Table 1).

Satisfactory analyses of MIs exposed at the surface of phenocrysts were obtained in only three of the five glass-bearing samples. The MIs are quite small (Fig. 1d) and many contain entrapped feldspars and/or micas making their analysis difficult. In MH1, once analyses contaminated with crystals and those showing abnormally low total (< 90 wt%) have been filtered out, eight analyses were retained. Normative compositions, A/CNK, A' and B' calculated on these MI are constant despite EMPA totals being somewhat variable and, therefore, their compositions have been averaged. In MA85-4, only one MI analysis could be retained whereas seven were obtained in CR85-2. On average, MIs have major element compositions almost identical to matrix glasses, being moderately silica-rich (~70-71 wt% SiO_2), strongly peraluminous (A/CNK = 1.21-1.33; A' = 48.5-72, normative corundum = 2.6-4.0%) and felsic (B' < 15, normative anorthite = 1.3-1.8%, Table 1; Fig. 2). The F concentrations in MIs are higher and totals slightly lower than in matrix glasses (Table 1). MIs in CR85-2 have K_2O higher than in the two other samples.

The new major element analyses of obsidian glasses JV2, JV3 and CH0 are reported in Table 1. The data are in very good agreement with the older analyses except for Na_2O and K_2O in CH0, erroneously inverted in Table 2 of Pichavant et al. (1987). Obsidians JV2 and JV3 are more peraluminous (A/CNK = 1.41-1.44; A' = 90.6-99.6, normative corundum = 4.8-5.4%) and felsic (B' < 10, normative anorthite < 1.0%) than matrix glasses and MIs (Fig. 2), they also have higher F (1.33-1.89 wt%), P_2O_5 (0.56-0.67 wt%) and normative albite contents (36-39%). JV3 has the most evolved major element composition. CH0 differs from the two other obsidians in having a very low normative quartz content (24 vs. 32-35% in JV2 and JV3) and being less peraluminous (A/CNK = 1.22 vs. ~1.40 in JV2 and JV3, Table 1; Fig. 2). This confirms the marked compositional differences between the Chapi (CH0) and the Caluyo Mayo and Chilcuno Chico (JV1, JV2, JV3) obsidians, as previously noted (Pichavant et al., 1987).

In the A'-B' diagram (Fig. 2, Debon and Le Fort, 1983), glass compositions plot in the upper left domain representative of felsic peraluminous silicic compositions (Pichavant et al., 1987; 1988b; Villaseca et al., 1998; Cuney, 2014). The glass data points are relatively grouped (notice the less peraluminous CH0 composition) and matrix and obsidian glasses plot respectively at the unevolved and evolved end of the glass range. Ash-flow tuffs plot clearly outside the glass domain, being markedly less felsic (i.e., higher B') than the least evolved matrix glasses (Fig. 2).

4.3. Major element compositions of mineral phases

Representative electron microprobe compositions of phenocrysts in the Macusani and Picotani samples are reported in the Data repository (Table S1). The new data are mostly for the glass-bearing samples but all glass-free samples were re-analyzed to standardize the LA ICP-MS data and compare between recent and older (Pichavant et al., 1988a) EMPA results. Overall, an excellent agreement was found between the two groups of data and some analyses from the older dataset are used in Table S1. The major element chemistry of mineral phases in

the Macusani Volcanics has been reported in detail in Pichavant et al. (1988a). The main points are recalled below while the new data are highlighted.

Quartz is close to end-member SiO_2, containing only minor (< 0.5 wt%) Al_2O_3 concentrations. CL imaging shows that growth zoning is common in phenocrysts from both Macusani and Picotani samples (these will be designated below as "zoned crystals", Fig. S1). In MA85-7 and MH6 (Macusani samples), several Qz phenocrysts (designated below as "composite crystals") show dark, homogeneous and rounded cores rimmed by zoned overgrowths (Fig. S1). Zoned and composite crystals have cores and rims with identical major element compositions (Table S1; Fig. S1). *Plagioclases* in Macusani ash-flow tuffs have been shown previously to divide in two main groups (Pichavant et al., 1988a). The group I includes most phenocrysts whereas the group II are restricted to Pl cores (Fig. S2). In the former, An ranges mainly from ~10 to ~15 with some up to 20 and in the latter from An ~30 to ~45 (Table S1; Fig. S2; Pichavant et al., 1988a). Both Pl groups display oscillatory zoning and the transition between cores (group II inclusions) and rims (group I overgrowths) is quite sharp (Fig. S2; Pichavant et al., 1988a). In the group I crystals, core-rim variations are < 10% An and both normal and reverse zoning can be encountered. The Picotani samples show no group II cores and Pl are slightly less An-rich (8-15, Table S1) than the group I in Macusani samples. *Sanidines*, either as isolated phenocrysts or inclusions in other major phases, are all very homogeneous, from Or ~68 to ~73 (Table S1; Pichavant et al., 1988a). CL imaging reveals common growth zoning. However, Af cores and rims have similar major element chemistries and analyses across the CL zonation show no systematic variations. Af major element compositions in Macusani and Picotani samples overlap. *Biotites* are all highly aluminous and Ti-bearing with Mg# (= at. Mg / (Mg + total Fe)) around 0.3 irrespective of texture (isolated phenocryst, partially reacted crystal, inclusion). Some compositions extend up to Mg# ≥ 0.35 and a few have Mg# as low as ~0.2 (Table S1; Pichavant et al., 1988a). The Picotani biotites have Mg# lower than most Macusani compositions. The F concentrations are quite irregular, up to ≥ 3 wt% in some samples (CHA85-10, -11, Table S1). *Muscovites* contain significant Ti, Fe, Mg concentrations and are systematically F-bearing to F-rich (Table S1; Pichavant et al., 1988a). They have Mg# between ~0.4 and ~0.5, the Macusani and Picotani compositions being respectively at the upper and lower end of the range. *Andalusite* and *sillimanite* are both close to stoichiometric Al_2SiO_5 (Table S1; Pichavant et al., 1988a). *Tourmaline,* either as isolated phenocrysts or inclusions in major phases, has Mg# around 0.3 and shows weak core-to-rim zonation (Table S1, Pichavant et al., 1988a). *Ilmenites* (Macusani samples) have variable Mn, low Al and Mg and detectable Zn. Proportions of hematite (Fe_2O_3) are very low (< 1%, Table S1, Pichavant et al., 1988a). Many Ilm exhibit excess Ti (Pichavant et al., 1988a and references therein) and low totals, as low as 92 wt% (Table S1). In comparison, inclusions in biotite reaction zones (samples CHA2, CHA85-10, -11) have high but normal Ti and totals around 100 wt%. *Hercynites* are very Zn-rich with variable but elevated amounts (up to nearly 50%) of the gahnite component ($ZnAl_2O_4$) and low Fe_2O_3/FeO (Table S1; Pichavant et al., 1988a).

4.4. Trace element compositions of glasses

Trace element concentrations in standard glasses and obsidians are reported in Table 2. Repeated analysis of external standard NIST610 showed agreement within +/-1 ppm with reference values. For BCR-2G, deviations from reference values are < 20% for most elements and up to 20-30% for Nb, Sn and Ta. A large number of analyses is available on JV2 and CH0

obsidians as both served as quality control during the data acquisition period. In contrast, JV1 and JV3 were analyzed less systematically. Since all available analyses have been averaged, the analytical variability is maximized for JV2 and CH0, standard deviations (s.d.) and analytical errors (1 σ) being in the same range or within a factor 2 (Table 2). In comparison, standard deviations for JV1 and JV3 are much lower than analytical errors since the number of analyses is relatively small (Table 2). Analytical dispersions in obsidians (RSD, Table 2) are in general < 20%, increasing with decreasing concentration. Elements in the ppm range or less such as Ge (in JV2), Sr, Ba and the REE have RSD up to > 50% (JV2, Table 2).

The LA ICP-MS results on JV1 and JV2 are, for most elements, within 20% of the previous data (Pichavant et al., 1987). However, Zr, the REE, Pb, U have LA ICP-MS concentrations systematically lower (by 20-60%) than the reference values (Table 2). This is due to the presence of zircon and monazite microcrystals in obsidians (Pichavant et al., 1987; 1988a). Although these phases were carefully avoided during LA ICP-MS analysis, they were incorporated in reference values since bulk analytical methods were used (ICP-ES, XRF, Pichavant et al., 1987). Another element systematically depleted (by ~30%) in JV1 and JV2 compared to the reference INAA data (Pichavant et al., 1987, Table 2) is Ta. ^{181}Ta exhibits extreme negative laser induced element fractionation in comparison with Si[29] (Jenner and Arevalo, 2016) and this might explain the relatively low Ta concentrations measured in obsidians.

The new data for JV1 and JV2 confirm the strong trace element enrichments and depletions found previously in Macusani obsidians (Pichavant et al., 1987); additionally, we note the first accurate values for Ba in JV1 and JV2 (1.1 ppm, Table 2). Together with major element analyses and F concentrations (Table 1; Pichavant et al., 1987), these data indicate that JV3 and CH0 are the two most chemically evolved obsidians. Both are enriched in Be, B, P, Rb, Sn, Cs, Ta and W relatively to JV1 and JV2 (Table 2). Yet, Li is markedly depleted in CH0 when compared to the other obsidians and P is also less enriched in CH0 than in JV3 (Table 2). Zn and Nb are equal or decrease slightly whereas Zr, La and U decrease from JV1 and JV2 to JV3 and CH0 (Table 2; Fig. 3). CH0 has Sr, Ba and Pb concentrations systematically slightly higher than in JV1 and JV2 (Table 2; Fig. 3).

The trace element compositions of matrix glasses are reported in Table 3. Glasses from the two Picotani samples are very homogeneous. Standard deviations are lower or in the same range than analytical errors for practically all elements and RSD are < 20% irrespective of the concentration level (i.e., 0.1-1 ppm for the REE, Table 3). The three Macusani matrix glasses are less homogeneous. Standard deviations exceed errors for some elements in MA85-4 and MA85-7 and for all in MH1. The RSD are > 20% for Zn, Sr, Ba, being systematically up to ~50-60% for the REE in MA85-4 and MA85-7 (Table 3). These heterogeneities are of analytical nature, i.e., they reflect the relatively small size and bubbly nature of the glass filaments analyzed in the Macusani samples (Fig. 1b). In contrast, for the Picotani samples, the larger and denser matrix glass domains (Fig. 1c) allowed for more reproductible ablation signals to be obtained. For Li, B, P, Rb, Nb, Sn, Cs, Ta and W, concentrations increase from matrix glasses to obsidians (e.g., Li, B and Ta, Fig. 3a; c; d) whereas, for Be and Zn, the data overlap, i.e., the most enriched matrix glasses reach concentrations in the range of obsidians (Fig. 3b). In contrast, Zr, La and U concentrations decrease slightly from matrix glasses to obsidians (Fig. 3e) whereas the Sr, Ba and Pb decrease more markedly (Fig. 3f). Li, B, Zn, Cs, Ta and W matrix glass concentrations overlap between the two volcanic fields but the Picotani have higher Be, P and Sn and lower Sr, Zr, Nb, Ba, La, Pb and U than the Macusani glasses (Fig. 3). Among the latter, the MH1 matrix glass is the most evolved, being enriched in Li, Be, B, P, Rb, Cs, Ba,

Ta and W, equal in Zn, Sr, Nb and Pb and depleted in Sn and U (Table 3) relative to MA85-4 and MA85-7.

Glass inclusions (MIs) have been reliably analyzed for trace elements in only two samples. Compositions of nine MIs, all analyzed at the surface of Qz, are available for MH1 (Table 4). Seven define a group of compositions close to the MH1 matrix glass. Two inclusions stand out of the main group, having much higher Li (~2500 ppm vs. ~700 ppm) and also higher Zn, Zr, La and U and lower Be, B, Nb, Cs, Ta and W (Fig. 4; Table 4) suggesting trapping of two chemically similar but independent melts. Within the main group, Li and Sn are the two most heterogeneously distributed elements (s.d. > 1 σ; RSD > 20%; Table 4). Relative to the matrix glass average, Sn is strongly enriched in MIs and Zn moderately so whereas Sr and Ba are both depleted (Fig. 4d; f). In sample CR85-2, three MIs at the surface of Qz and one at the surface of Af were analyzed (Table 4), the data being less homogeneous than in MH1. Standard deviations exceed analytical errors for several elements and Li, Be, Ti, Ba and Sm have RSD well above 20% (Table 4, Fig. 4b). Average MI and matrix glass concentrations are within 20% of each other except for Li and Ba (depleted in inclusions) and Rb, Cs, Eu and U (enriched in inclusions Table 3; 4; Fig. 4a).

4.5. Trace element compositions of mineral phases

Most mineral phases have been analyzed for trace elements except for apatite and cordierite. Apatite is a minor but systematic phase both in the Macusani and Picotani samples but is commonly full of Ilm, Sill, Mz and Zrc inclusions (Pichavant et al., 1988a) which makes LA ICP-MS analysis difficult. Apatite concentrates the REE, Y, Sr but not U, Th, Pb and the lithophile elements (Prowatke and Klemme, 2006). However, as the latter elements are the focus of this study, analysis of apatite was not considered as a necessity. Cordierite phenocrysts in Macusani samples are systematically pseudomorphosed by alteration products such as pinite and beidellite-nontronite (Pichavant et al., 1988a), thus no attempt was made to determine their trace element concentrations.

Quartz. Trace element concentrations in Qz phenocrysts (59 analyses) are compiled in Table S2 (Data repository). Qz contains significant Li (47-198 ppm), Al (208-886 ppm) and Ti (12-73 ppm) with P mostly in the 5-10 ppm range (Table S2) and Ge and other elements variably low and mostly < 1 ppm. The data are consistent with Li incorporation in Qz according to the coupled substitution Al = Li at. (Müller and Koch-Müller, 2009) although we note a few analyses plotting below the 1:1 reference line (Fig. 5). Qz compositions in glass-bearing and glass-free samples overlap but the most Li-rich are found in the MH2, MH4 and MH7 glass-free samples (Fig. 5; Table S2). Cores and rims of zoned crystals do not show systematically contrasted trace element concentrations. Yet, the cores of composite crystals (MA85-7, MH6, Table S2) have the lowest Li and Al and they plot separately from the main compositional group (Fig. 5).

Plagioclase. The 40 available analyses are provided in Table S2. Pl phenocrysts cover a wide compositional range (Fig. 6; 7; Table S2). Three main types of Pl compositions are apparent in the An vs. Sr, Ba plots. The first, numerically the larger and with An < 20, has Sr < 300 ppm and Ba < 100 ppm and it corresponds to the group I Pl (Fig. 6). It is characterized by P, Rb progressively increasing and Mn, Ba, La, Eu and Pb decreasing with decreasing Sr (Fig.

7). Ti and Zn are constant and Be and B show broad positive correlations. Li concentrations vary by as much as half an order of magnitude (from ~200 to ~900 ppm), especially in the glass-free samples (Fig. 7d). Sn is also quite variable with values mostly around ~5 ppm or less and a few up to 20 ppm (Table S2).

The second compositional type (An = 35-40, Sr = 500-1200 ppm, Ba = 100-250 ppm) corresponds to group II Pl (Fig. 6). Qualitative LA ICP-MS line scans across a complex feldspar phenocryst show that the transition from group I to group II compositions is marked by a sharp increase in Sr, Ba, La and Eu (Fig. S3) and a slight decrease in Rb. Individual analyses of group II Pl plot at the high end (less evolved) parts of Sr evolution trends, have high Ba, La, Eu and Pb and some also show spikes in Mn and Zn concentrations (Table S2).

Six analyses, of which four are from MA85-4, show major and trace element signatures that equate neither group I nor group II Pl (Fig. 6). They have very high Sr (427-1718 ppm) and Ba (38-706 ppm) and include the three analyses with the highest Sr and Ba in the Pl database (6, MH1; 14, MA85-4; 36, MH3 in Table S2). The MH3 analysis has also the highest Ti, La and Eu and very low Be, B, Zn and Sn (Table S2). Although these analyses share with group II Pl high Sr, Ba and REE, their An contents are lower (15-26) and intermediate between group II and group I Pl (Table S1; Pichavant et al., 1988a). These data suggest that these Pl define a distinct population (group III) so far unidentified from textures and major elements.

The trace element compositions for Pl in glass-bearing and glass-free samples do not show systematic differences, except for Li discussed above (Fig. 7d). The data for Pl in the Macusani and Picotani glass-bearing samples overlap although the former cover much wider compositional ranges than the latter (Fig. 6; 7). The less evolved Pl compositions (at high end of Sr evolution trends) only come from Macusani samples (Fig. 7). The Picotani Pl, together with other Macusani compositions, plot at low end of Sr trends (Fig. 7a; b; c, Table S2).

Sanidine. A total of 44 analyses are available (Table S2). Cores and rims of zoned crystals do not show systematic differences (Table S2) although regular trends appear for most elements when the entire database is considered. Sr, Ba, La, Eu and Pb progressively decrease while Be, B, P, Mn, Sn and Cs increase with increasing Rb (Fig. 8a; b; c). Li behaves irregularly and the highest Li concentrations come from the glass-free samples (Fig. 8d). Apart from Li, Af from glass-bearing and glass-free samples have similar trace element compositions. Those from the Macusani glass-bearing samples span the full compositional range. In contrast, analyses from the Picotani samples plot in the intermediate to evolved range of Rb trends (Fig. 8). The four analyses at the low ends (2 from MA85-4 and 2 from MA85-7) are specific. One (17, MA85-7, Table S2) has exceptionally high Sr, Ba, Eu and exceptionally low B, Be, Li, Cs. The three others also show high Sr, Eu and low B, Cs while Ba, Be, Li are more variable and Mn is higher than the main group (Fig. 8).

Biotite. 49 analyses are available (Table S2). Compositions do not vary systematically across grains except for one core analysis highly enriched in B, P and depleted in Li, Rb, Zn, Nb, Ta relative to the rim (g to l, MH1, Table S2; Fig. 1a). The Mg# and most trace elements correlate with the Rb concentration (Fig. 9). Li, Be, B, P, Mn, Zn, Nb, Sn, Cs, Ta and W all increase and Sr, Ba and Pb decrease with increasing Rb. Particularly strong positive correlations are noted for Cs and Ta while Mn, Nb, Sn and W are more dispersed and Zn is almost constant with Rb (Fig. 9b, Table S2). A partially reacted biotite inclusion in a group II Pl core has one of the lowest Rb values, relatively high Li and very elevated Be (analysis b, CHA2, Table S2). Other partially reacted biotites in CHA85-10 and CHA85-11 have Nb and Ta slightly higher than the other analyses (Fig. 9b, Table S2). Several samples contain Biot with low Rb (~1000

ppm) and Ba concentrations (> 800 ppm and up to 1868 ppm) well above the main group (~200 ppm, Fig. 9d, Table S2).

Trace element compositions of biotites do not systematically differ between glass-bearing and glass-free samples except for Li preferentially enriched in the latter (Fig. 9c). Biot from Macusani samples cover the whole range of compositions, from unevolved (MA85-4, MH8), intermediate (MA85-7, MH4, CHA85-10, CHA85-11) to highly evolved (MH1, MH7). The Picotani Biot are more evolved (higher Rb) and they have similar Rb, Be, B, P and Nb, lower Li, Sr, Sn, Cs, Ta and W and higher Zn than the most evolved Macusani Biot (Fig. 9, Table S2). The Ta and W vs. Rb trends for the Macusani (MH1) and the Picotani biotites appear distinct (Fig. 9c, Table S2).

Muscovite. Fewer analyses are available (16, Table S2) than for the other major phases since Mu phenocrysts are not present in all samples. Compositions, although quite homogeneous in a given sample, span a substantial range of trace element concentrations (Fig. 10, Table S2). Li, Be, B, Mn, Zn, Nb, Sn, Cs, Ta and W all increase with increasing Rb while Mg# and Sr decrease (Fig. 10). The least and most evolved muscovite compositions come from the Macusani glass-free samples (respectively MH7, MH2 and MH3) while the glass-bearing samples are intermediate, the Macusani being more enriched in Be, Sr, Sn, Cs, Ba and W than the Picotani Mu (Fig. 10, Table S2).

Tourmaline. This phase has been analyzed in only two glass-free samples (MH3, MH7, Table S2). Li, Mn and Zn are up to several 100 ppm whereas Be, Sr, Sn and Pb are in the several to ~10 ppm range and Rb, Zr, Nb, Cs, La, Ta and W are mostly < 1 ppm. There is no systematic variation in trace element concentrations with position in the crystal (Table S2), consistent with the near lack of major element zonation in tourmaline (Pichavant et al., 1988a).

Andalusite. Six analyses are available for this phase, four in glass-bearing (MH1) and two in glass-free (MH2 and MH3) samples. It contains elevated P (87-222 ppm) and has Li, B, Mn, Zn and Sn in the several ppm to ~10 ppm range (Table S2). Most Be, Nb, Cs, Ta and W concentrations are < 1 ppm.

Ilmenite. A total of 13 analyses are available all but one being for phenocrysts in the Macusani glass-bearing samples (Table S3, Data repository). Mn concentrations are high (several ten thousand ppm) and variable (see also Table S1 and Pichavant et al., 1988a), being positively correlated with Zn, Nb, Sn and Ta but not with W (Table S3). Li is surprisingly high (from < 50 and up to > 1000 ppm) and strongly positively correlated with the Mn content (Table S3). Phenocrysts from MH1 are the most Mn- and Li-rich and they also have compositions distinct from those in MA85-4 and MA85-7 (Table S3). Ilm from a biotite reaction zone is similar to the phenocrysts (Table S3).

Hercynite. Inclusions in biotite reaction zones (see Pichavant et al., 1988a for textural details) have been analyzed in three Macusani glass-free samples (Table S3). As expected, Hc has very high Zn (see also Table S1 and Pichavant et al., 1988a) whereas Mn is in the 1000 ppm and Ti in the x100 ppm range. The Li concentrations are grouped around ~100 ppm in the 4 analyses available, Be being at the ppm level (Table S3). Hercynites do not concentrate rare-metals such as Nb, Sn, Ta and W which are all < 1 ppm (Table S3). Be, Ti and Mn decrease with increasing Zn and no significant correlation appears between Li and Mn at the difference of ilmenite (see above).

5. Mineral/melt partitioning

5.1. Identification of equilibrium mineral assemblages

Derivation of mineral/melt partition coefficients requires identification of mineral assemblages in equilibrium with residual melts represented by matrix glasses. This is straightforward for the Picotani samples which are relatively simple mineralogically, as noted previously. However, the Macusani samples are more complex. Two distinct stages, early and late magmatic, have been distinguished in the pre-eruptive evolution of Macusani ash-flow tuffs (Pichavant et al., 1988a). The early stage, characterized by Sill, group II Pl, Biot reacted to Hc, Cd, Tur and most accessory phases, comprises restites and/or early phenocrysts and is representative of conditions within or near the magma source region (Pichavant et al., 1988a). The low Li, Al cores imaged by CL in Qz composite crystals (Fig. S1) are interpreted as residual phases and so a partly restitic origin is implied also for Qz. By opposite, no residual Af is present according to CL and trace element data. The group III Pl identified from trace element signatures in this study are interpreted as rare low An equivalents of the group II. The late stage, which corresponds to magma crystallization and pre-eruptive equilibration in subvolcanic reservoirs, is characterized by Qz, Af, group I Pl, Biot, Mu, And, Ilm, an assemblage similar to that of Picotani samples (Qz, Af, Pl, Biot, Mu). The early and late stages are strongly contrasted mineralogically (i.e., Sill vs. And and group II vs. group I Pl), the two respective assemblages corresponding to distinct conditions of temperature (~800 vs. ~650°C), pressure (400-500 vs. 150-200 MPa) and melt water contents (4-5 vs. 4.5-6 wt% H_2O, Pichavant et al., 1988a). The late magmatic phases largely dominate volumetrically as they mark the main crystallization stage of the magmas. The early magmatic phases are found in specific textures (group II Pl, reacted Biot), as minor phenocrysts and inclusions (Pichavant et al., 1988a). In the following, only late magmatic phases will serve for the calculation of mineral/melt partition coefficients.

5.2. Compositional variability in glasses and phenocrysts

Determination of partition coefficients requires trace element concentrations in phenocrysts and glasses coexisting at equilibrium. Matrix glasses from this study are homogeneous in major and trace elements for a given sample and, therefore, average matrix glass compositions have been used in the calculations below. As a test of the influence of glass composition, calculations were also performed using the average of glass inclusions in MH1 and CR85-2 and the average of the two most Li-rich inclusions in MH1.

In contrast, phenocrysts have variable major and trace element chemistries. Variations in Qz, group I Pl, Af, Biot, Mu (Figs. 5-10) and Ilm (Table S3) compositions are systematic. Macusani and Picotani are examples of two separate long-lived large volume periodically recharged and erupted igneous systems. Recharge magmas were generated under similar but specific conditions in the anatectic region (as shown by the homogeneous compositions of ash-flow tuffs, Fig. 2). Each batch crystallized under P-T-H_2O melt slightly different from each other (to account for the variable modal proportions of phenocrysts between ash-flow tuffs,

Pichavant et al., 1988a). Therefore, melts and phenocrysts with compositions in the same *range* but variable in detail coexisted within the reservoirs. The phenocryst trace element data (Figs. 5-10) provide a record of the chemical variability between recharge magmas.

The glass-bearing samples used for the calculation of partition coefficients cover a subset of the global phenocryst variability. However, chemical heterogeneities exist down to the thin section scale. For Qz, no clear trace element core-rim zonation was observed and, in a given sample, the range of concentrations is wider than the core-rim variability (e.g., MA85-4, CR85-1, Table S2). Similarly, normal core-rim zonation in Af (i.e., decrease of Ba with increasing Rb) is rarely well marked (e.g., CR85-2, Table S2). Both unzoned and inversely zoned phenocrysts are present; core and rim trace element concentrations overlap in a given sample (e.g., MH2, MH6, Table S2). For the group I Pl phenocrysts, the trace element zonation (Ba and Sr decrease from core to rim, Fig. 6) is more clearly marked (e.g., 15, 16 in MA85-7, Table S2) although core and rim compositions in glass-bearing samples overlap. For Biot and Ilm, phenocrysts with slightly different compositions coexist in the same thin section and core-rim zonation is exceptional whereas Mu are more grouped (Table S2). These observations suggest that the chemical variability at the thin section scale is mainly due to mixing between phenocrysts with different magmatic histories. Only some group I Pl record crystallization and magma equilibration. The variability in phenocryst compositions at the thin section scale and the lack of systematic differences between cores and rims make difficult to identify analyses representative of equilibration with the matrix glass. Therefore, both core and rim analyses of phenocrysts have been considered in the calculation of partition coefficients. In complement, sensitivity tests have been performed to evaluate the impact of core compositions on the calculated K_d.

5.3. Calculation of phenocryst/melt partition coefficients

Partition coefficients (K_d) have been calculated from trace element concentrations in phenocrysts divided by trace element concentrations in glasses. For each glass-bearing sample, partition coefficients are calculated as $K_d = C_{Ph} / C_L$ where C_{Ph} is the concentration of a given element in a given phenocryst analysis and C_L the average of glass analyses (constant for a given element and glass-bearing sample). Then, the calculation is repeated for the other C_{Ph} available in the sample. Finally, the procedure is extended to the other glass-bearing samples and a set of K_d for a given phenocryst is obtained, which includes minima, maxima and median values (instead of averages to avoid giving too much weight to extrema). Relative errors on partition coefficients (σ_{Kd} / K_d) are obtained from the relation:

$$\sigma_{Kd} / K_d = 100*(\sigma_{Ph} / C_{Ph} + \sigma_L / C_L) \quad (1)$$

where σ_{Kd}, σ_{Ph} and σ_L are the absolute errors on K_d, C_{Ph} and C_L respectively. For a given element and phenocryst, σ_{Ph} is the 1 σ error (calculated with Glitter, Table S2; S3 and variable with C_{Ph}) whereas σ_L is the standard deviation of glass analyses (constant in a given glass-bearing sample, Table 3; 4). Equation (1) is applied to the different C_{Ph} and σ_{Ph} available and median relative errors on partition coefficients are calculated and discussed.

5.4. Mineral/melt partitioning results

Median K_d calculated for Qz, Pl, Af, Biot, Mu, And and Ilm are summarized in Table 5 and the different calculations are detailed on a phase-by-phase basis in Table S4 (Supplementary material).

Quartz. A total of 17 C_{Ph} are available for the glass-bearing samples. All available analyses except one (core in a composite crystal, 12 in MA85-7, Table 2) have been used and the results (noted $K_d(element)^{Qz/L}$) are illustrated in Fig. 11. The median $K_d(Al)^{Qz/L}$, $K_d(P)^{Qz/L}$, $K_d(Ti)^{Qz/L}$ and $K_d(Ge)^{Qz/L}$ are 0.005, 0.005, 0.14 and 0.20 (Table 5), Li being discussed separately below. For Al and Ti, partition coefficients calculated using matrix glasses and MIs are in the same range (Table S4). Compared to topaz rhyolites, K_d from this study are lower for B and P, in the same range for Ti and higher for Al (n.b., $K_d(Al)^{Qz/L} = 0$ in Dailey et al., 2018). The $K_d(REE)^{Qz/L}$ (between 10^{-3} and $< 10^{-1}$) are associated with large relative errors (> 70%, Table 5). Nb, Ta and U ($K_d \sim 10^{-4}$) are followed by Mn, Rb, Zr, Cs and W ($K_d = 10^{-4}$ -10^{-3}) and then Sr, Sn, Ba and Pb ($K_d = 10^{-3}$ -10^{-2}) in order of increasing compatibility (Fig. 11).

Plagioclase. A total of 11 group I Pl C_{Ph} are available. The two cores with the highest Ba and Sr in MH1 and MA85-7 (Table S2) have been kept since eliminating those analyses causes only minor changes on K_d (e.g., 2.81 instead of 2.98 for $K_d(Pb)^{Af/L}$, Table 5). Results from matrix glasses and glass inclusions globally overlap (see Table S4). Sr and Eu have the two highest K_d (Fig. 11). The $K_d(Sr)^{Pl/L}$ (median = 10.8, Table 5) is in good agreement with rhyolitic magmas whereas the $K_d(Eu)^{Pl/L}$ (median = 17.9, Table 5) is slightly above the references (Fig. 11; Ren et al., 2003). The grouping of Eu with other 2+ cations such as Sr and Ca in K_d vs. ionic radius plots (Onuma et al., 1968; Fig. 12) suggests Eu incorporation mainly as Eu^{2+}. The other 2+ cations entering the M site have lower K_d (Fig. 12). For the large cations, the $K_d(Ba)^{Pl/L}$ (0.87, Table 5) is in good agreement with the references, the $K_d(Pb)^{Pl/L}$ (Table 5) being slightly higher (Fig. 11; Ren et al., 2003). The small 2+ cations (Mn, Zn, Sn) have $K_d \sim 10^{-1}$ (Fig. 11). For the 1+ cations in the M site (Rb, Cs, Li being discussed separately), the K_d are in the 10^{-2} to 10^{-3} range and lower than in references (Table 5; Fig. 11). However, in the latter studies, the $K_d(Cs)^{Pl/L}$ plot well above the other 1+ cations in Onuma diagrams (see Padilla and Gualda, 2016; Dailey et al., 2018; Fig. 12). The 3+ RE cations (La, Sm, Gd, Yb) follow the expected increase in K_d with increasing ionic radius whereas Eu plots well above the trend (Fig. 12; Padilla and Gualda, 2016), our K_d being generally higher than in reference studies (Fig. 11; Ren et al., 2003). The $K_d(La)^{Pl/L}$ (3.57, Table 5) implies a compatible behavior in plagioclase that contrasts with the literature (Fig. 11; Ren et al., 2003). Yet, Congdon and Nash (1991) reported a $K_d(La)^{Pl/L} \sim 1$ for the Honeycomb Hills rhyolite and we note that La follows the other compatible elements (Sr, Ba) at the transition from group I to group II Pl (Fig. S3). The high K_d found in this study for the 3+ Rare Earth cations are attributed to mechanisms involving the plagioclase structure since these elements occur at trace levels in matrix glasses (< 5 ppm, Table 3). REE partitioning in plagioclase is controlled by substitution mechanisms involving Na and Ca in the M site and Si and Al in the T site (Bindeman and Davis, 2000). Plagioclases in the Macusani and Picotani igneous systems have strongly specific chemistries (P-rich with a slight Al excess and Si deficit in T site, Table S1) and the charge deficiency caused by Al = Si substitution might favor the preferential incorporation of 3+ cations in the M site. Last, the high field strength elements (HFSE, Zr, Nb, Ta, W, U) are strongly rejected from the plagioclase M site. They show $K_d < 10^{-2}$ (Table 5) consistently lower than in reference magmas, particularly topaz rhyolites (Fig. 11). Melts in Macusani and Picotani volcanics are globally more evolved

(higher Li, B, P, A/CNK) than in topaz rhyolites and the lower K_d observed in this study might reflect the influence of these elements on stabilizing the HFSE in silicic melts (Linnen, 1998).

Cations entering the T site, either 4+ (Ti, Ge) or 2+ (Be) have K_d in agreement with reference studies (Fig. 11; Fig. 12). P is significantly partitioned toward plagioclase ($K_d(P)^{Pl/L}$ = 0.61, Table 5). In contrast, the $K_d(B)^{Pl/L}$ is very low (3.10^{-3}, Table 5) and much lower than in topaz rhyolites (Fig. 11). This is due to the dominant trigonal coordination of B in peraluminous melts according to NMR data on Macusani obsidians (J. F. Stebbins, personal communication, 2023) which would impede B = Al substitution in the T site. Moreover, Al = Si substitution is promoted by the peraluminous melt chemistry and the elevated P melt concentrations (Table 3) further enhances Al incorporation through the Al + P = 2 Si coupled substitution (Simpson, 1977). This is confirmed by the composition of Macusani and Picotani plagioclases which, besides being P-rich, are characterized by slight Al excesses and Si deficits (Table S1). These different factors favor Al and conversely limit B incorporation in plagioclases from this study.

Sanidine. The four low Rb analyses have been filtered out leaving a total of 12 C_{Ph}. The three cores in MH1 have been kept despite having compositions slightly outside the main range for Af phenocrysts (Table S2). Removing those analyses causes only minor changes on K_d (e.g., 32.3 instead of 33.0 for $K_d(Ba)^{Af/L}$, Table 5). Results using average matrix glasses and the average of glass inclusions in MH1 and CR85-2 are globally in agreement (Table S4). The 2+ cations Sr, Ba, Eu strongly partition into the sanidine M site as found in previous studies (Ren, 2004; Bachmann et al., 2005; Padilla and Gualda, 2016; Dailey et al., 2018). Our $K_d(Sr)^{Af/L}$ (8.87, Table 5), reference values (Fig. 11; Ren, 2004) and experimental determinations (Icenhower and London, 1996) overlap. The $K_d(Ba)^{Af/L}$ (33.0, Table 5) is the highest for sanidine and slightly higher than in reference magmas (Fig. 11; Ren, 2004) and experimental results (Icenhower and London, 1996) although similar values (20-50) exist in the literature (Stix and Gorton, 1990 and references therein). Similarly, $K_d(Eu)^{Af/L}$ (16.8, Table 5) and $K_d(Pb)^{Af/L}$ (5.68, Table 5) appear both higher than reference values (Fig. 11; Ren, 2004). Changes in the order of compatibility from Eu > Sr > Ba in plagioclase to Ba > Eu > Sr in sanidine is consistent with the increase of the "ideal" ionic radius (the radius at the maximum partitioning in K_d vs. ionic radius regressions, Fig. 12) from the former to the latter (Fig. 12; Padilla and Gualda, 2016). The small 2+ cations (Mn, Zn, Sn) have K_d ~10^{-1} on average (Fig. 11). The 1+ cations (Rb, Cs, Li being discussed separately) are more compatible in sanidine than in plagioclase and their K_d agree with reference studies (Table 5; Fig. 11; Ren, 2004). Incorporation of these large 1+ cations is promoted by the increased "ideal" ionic radius for substitution in the sanidine M site (Fig. 12). The $K_d(La)^{Af/L}$ (0.34, Table 5) is slightly above the reference values (Fig. 11; Ren, 2004) whereas the $K_d(Gd)^{Af/L}$ is slightly below and the $K_d(Sm)^{Af/L}$ is in the same range (and lower than the $K_d(Gd)^{Af/L}$) but we note the large relative errors on K_d for the last two elements (> 100%, Table 5). Thus, for sanidine and in contrast with plagioclase, the 3+ cations do not have higher K_d than in reference magmas, most probably because their incorporation is more difficult with the increase of the "ideal" ionic radius for the M site. However, more differences are noted for Ba, Eu, Pb. The slightly higher $K_d(Ba)^{Af/L}$ compared to reference studies is unlikely to be explained by substitution mechanisms involving other trace elements since Ba is the trace cation that best fits incorporation in the M site (Ren, 2004; Padilla and Gualda, 2016; Fig. 12). $K_d(Ba)^{Af/L}$ positively correlates with Or in sanidine (Icenhower and London, 1996; Ren, 2004) and we attribute the preferential Ba incorporation in sanidine to substitution mechanisms involving the major elements (Icenhower and London, 1996) rather than to melt structure. For Eu, the dominant presence of Eu^{2+} (as suggested by the grouping of Eu with other 2+ cations in Onuma diagrams, Fig. 12) might explain the high $K_d(Eu)^{Af/L}$ (and also the high $K_d(Eu)^{Pl/L}$). Concerning Pb, both the Peach Spring Tuff and topaz rhyolites have anomalously low K_d for feldspars in comparison with the other 2+ cations

(Padilla and Gualda, 2016; Dailey et al., 2018, Fig. 12) and our K_d values seem preferable (Fig. 11). Last, the very low K_d (< 10^{-3}, Table 5) for Zr, Nb, Ta, W, U in sanidine, consistently lower than in reference magmas (Fig. 11) are, as for plagioclase, interpreted to result from the stabilization of HFSE in evolved Macusani and Picotani melts.

Cation incorporation in the sanidine T site is very similar to that in plagioclase (Fig. 12). The $K_d(Be)^{Af/L}$, $K_d(Ti)^{Af/L}$ and $K_d(Ge)^{Af/L}$ agree with the reference examples (Fig. 11) and, together with P ($K_d(P)^{Af/L}$ = 0.81), all are very close to in plagioclase (Table 5). B shows the same behavior in sanidine than in plagioclase. The $K_d(B)^{Af/L}$ is very low (2.10^{-3}, Table 5) and in marked contrast with topaz rhyolites (Fig. 11). The interpretation proposed above for plagioclases also holds for sanidines which are P-rich and show Al excesses and Si deficits (Table S1).

Biotite. The two high Ba (> 600 ppm) low Rb (~1000 ppm) analyses in MA85-4 (Fig. 9d) have been discarded, leaving 26 C_{Ph}. The core composition in MH1 has been kept in the calculations since its exclusion does not appreciably change the results (e.g., $K_d(Ba)^{Biot/L}$ = 5.12 vs. 5.02, Table 5). K_d calculations performed with matrix glasses and glass inclusions in MH1 and CR85-2 do not significantly differ from each other (Table S4). Ti and Mg are the two most compatible elements in the biotite octahedral (M) site (Fig. 11 and S5). The $K_d(Ti)^{Biot/L}$ is very high (93, Table 5), the EMPA (Table 1 and S1) and the LA ICP-MS analyses (Table 3 and S2) yielding almost identical averages. In comparison, most literature $K_d(Ti)^{Biot/L}$ are lower (~20), whether derived from rhyolitic magmas (Padilla and Gualda, 2016) or partitioning experiments (Icenhower and London, 1995; Were and Keppler, 2021). In partial melting experiments, peritectic biotites chemically close to those in the present study (apart for the lack of F and higher Mg#) have $K_d(Ti)^{Biot/L}$ ~30 (Michaud et al., 2021). In crustal anatectic environments (El Hoyazo enclaves), $K_d(Ti)^{Biot/L}$ ranges from 26 (calculations using matrix glasses) to 111 (calculations using glass inclusions, Acosta-Vigil et al., 2010). Previous works on Ti incorporation in biotite have stressed the importance of the mica crystal chemistry and of coupled substitutions with major elements and Ba (Icenhower and London, 1995; Waters and Charnley, 2002; Cesare et al., 2003). Therefore, our high $K_d(Ti)^{Biot/L}$ is interpreted to be the consequence of the chemical specificity (high Al and F, low Mg#) of biotites in the Macusani and Picotani volcanics. The high $K_d(Mg)^{Biot/L}$ (101, Fig. 12) is intermediate between values in rhyolitic magmas (260, Padilla and Gualda, 2016) and in experiments (~50, Icenhower and London, 1995; Were and Keppler, 2021). For the transition metals, the $K_d(Mn)^{Biot/L}$ (median = 4.12, Table 5) is in good agreement with experimental determinations (3-4, Icenhower and London, 1995) but lower than in the Peach Spring Tuff (13, Padilla and Gualda, 2016; Fig. 11) whereas the reverse is observed for the $K_d(Zn)^{Biot/L}$ (18.8, Table 5, vs. 18 in rhyolitic magmas, Fig. 11 and 5.8 in experiments, Were and Keppler, 2021). The $K_d(Sn)^{Biot/L}$ (0.44, Table 5) is in good agreement with topaz rhyolites (Fig. 11). Other elements compatible in the biotite M site include Nb and Ta. The $K_d(Nb)^{Biot/L}$ and $K_d(Ta)^{Biot/L}$ (9.75 and 2.35, Table 5) are respectively slightly above and below those in El Hoyazo enclaves (4.9-9.2 and 2.6-3.9, Stepanov and Hermann, 2013). In contrast, rhyolitic magmas ($K_d(Nb)^{Biot/L}$ and $K_d(Ta)^{Biot/L}$ = 1.56 and 0.45 in the Peach Canyon Tuff, Padilla and Gualda, 2016) and partitioning experiments consistently yield lower K_d (Were and Keppler, 2021; Gao et al., 2023), most probably because of marked differences in the respective Biot compositions. However, the elevated $K_d(Nb)^{Biot/L}$, $K_d(Ta)^{Biot/L}$ and $K_d(Ti)^{Biot/L}$ found in this study are mutually consistent (Gao et al., 2023). The REE have very low K_d (from 10^{-3} to 10^{-1}, Table 5) and the 3+ cations (La, Sm, Gd, Yb) show the expected K_d variations while Eu plots above the trend (Fig. 12). Our data are lower than in reference rhyolitic magmas (especially topaz rhyolites, Fig. 11) and in experiments (Were and Keppler, 2021) but close to the El Hoyazo enclaves (Acosta-Vigil et al., 2010). Such low K_d reflect the preferential stabilization of the 3+ RE cations in evolved Macusani and Picotani melts. U shows

the same type of behavior ($K_d(U)^{Biot/L}$ = 0.01) while Zr is more compatible ($K_d(Zr)^{Biot/L}$ = 0.14, Table 5) and slightly higher than in rhyolitic magmas (Fig. 11) but close to the El Hoyazo enclaves (Acosta-Vigil et al., 2010). W is also moderately incompatible ($K_d(W)^{Biot/L}$ = 0.38, Table 5), higher than in topaz rhyolites (0.06, Dailey et al., 2018; Fig. 11) but lower than in the Honeycomb Hills rhyolite (0.7-1.0, Congdon and Nash, 1991), the incorporation of W (and also Zr) in the M site being most probably controlled by the biotite chemistry.

Among the large 1+ cations partitioned into the biotite I site, K and Rb are the most compatible and Na the most incompatible while Cs is intermediate (Fig. 12). The $K_d(Rb)^{Biot/L}$ and $K_d(Cs)^{Biot/L}$ (respectively 2.87 and 0.46, Table 5) are both in good agreement with literature values, either from rhyolitic magmas (Fig. 11) or experiments (Icenhower and London, 1995; Were and Keppler, 2021). Ba is by far the 2+ cation the most compatible in the I site (Fig. 12). The $K_d(Ba)^{Biot/L}$ (5.02, Table 5) is in the low range of values for rhyolitic magmas (Fig. 11) but in agreement with the El Hoyazo enclaves (Acosta-Vigil et al., 2010) and experiments (Icenhower and London, 1995). Pb is less compatible and Sr and Ca are the most incompatible (Fig. 12). The $K_d(Pb)^{Biot/L}$ (0.24, Table 5) is in good agreement with reference values and the $K_d(Sr)^{Biot/L}$ (0.11, Table 5) is in the same range as in experiments (Icenhower and London, 1995) while values for rhyolitic magmas show a significant variability (Fig. 11).

B ($K_d(B)^{Biot/L} = 4.10^{-3}$, Table 5) is the most incompatible of cations entering the T site (Fig. 12) and it shows the same difference with topaz rhyolites already discussed (Fig. 11). P ($K_d(P)^{Biot/L}$ = 0.06) is less partitioned in biotite than in feldspars (Table 5). The $K_d(Be)^{Biot/L}$ (0.06, Table 5) and the reference value overlap (Fig. 11), both being higher than in experiments (0.45, Evensen and London, 2002; 0.58, Pichavant et al., 2016; see the detailed comparison in Dailey et al., 2018).

Muscovite. A total of 10 C_{Ph} are available. As for biotite, Ti and Mg are the two most compatible elements entering the M site (Fig. 12). The $K_d(Ti)^{Mu/L}$ (19.8, Table 5) is in good agreement with the muscovite separate data on the Richemont rhyolite (18.8, Raimbault and Burnol, 1998; Fig. 13), both being higher than in experiments (6.7, Icenhower and London, 1995). Mg ($K_d(Mg)^{Mu/L}$ = 18.7, Fig. 12) and the transition metals are less strongly partitioned in muscovite than in biotite. The $K_d(Mn)^{Mu/L}$ (0.32) and the $K_d(Zn)^{Mu/L}$ (1.61, Table 5) are both lower than in the Richemont rhyolite (respectively 1.97 and 7.1, Raimbault and Burnol, 1998; Fig. 13) and, for Mn, lower than in experiments (1.2, Icenhower and London, 1995). Sn ($K_d(Sn)^{Mu/L}$ = 0.53, Table 5; 0.37, Raimbault and Burnol, 1998) contrasts with W which is compatible in muscovite ($K_d(W)^{Mu/L}$ = 2.1, Table 5; 2, Raimbault and Burnol, 1998). Nb is much more compatible than Ta ($K_d(Nb)^{Mu/L}$ = 4.30 vs. 3.5, $K_d(Ta)^{Mu/L}$ = 0.63 vs. 0.42 respectively in Table 5 and Raimbault and Burnol, 1998) so that muscovite crystallization preferentially enriches Ta in the residual melt (Stepanov et al., 2014). The 3+ RE cations (La, Sm, Gd, Yb) are the least easily incorporated in the muscovite M site, their K_d (10^{-3} - 10^{-2}, Table 5) regularly increasing with decreasing ionic radius (Fig. 12). As observed for biotite, the $K_d(Eu)^{Mu/L}$ (0.29, Table 5) is significantly higher than for the other REE (Fig. 13; Fig. 12). U behaves similarly to the 3+ RE and the $K_d(U)^{Mu/L}$ (0.01, Table 5) is lower than in the Richemont rhyolite (Fig. 13). In comparison, Zr is more compatible ($K_d(Zr)^{Mu/L}$ = 0.21, Table 5).

As in biotite, K and Rb are the two 1+ cations the most compatible in the muscovite I site, Cs being more incompatible than in biotite (Fig. 12). Both the $K_d(Rb)^{Mu/L}$ (1.75, Table 5) and the $K_d(Cs)^{Mu/L}$ (0.08, Table 5) are in quite good agreement with experiments (respectively 1.6 and 0.2, Icenhower and London, 1995) whereas the Richemont rhyolite yields slightly higher values (respectively 2.4 and 0.5, Raimbault and Burnol, 1998; Fig. 13). Ba is the most compatible 2+ cation in the I site (Fig. 12). The $K_d(Ba)^{Mu/L}$ (3.3, Table 5) compares well with

experimental values (4.5, Icenhower and London, 1995). Sr and Pb ($K_d(Sr)^{Mu/L}$ = 0.30, $K_d(Pb)^{Mu/L}$ = 0.23, Table 5) are both moderately incompatible in muscovite.

B ($K_d(B)^{Mu/L}$ = 0.04, Table 5) is concentrated in the muscovite T site in comparison with the other major phases whereas P partitions similarly than in biotite (Table 5). The $K_d(Be)^{Mu/L}$ (0.10, Table 5) is in the same range as in the Richemont rhyolite (0.24, Raimbault and Burnol, 1998) but we note the higher $K_d(Be)^{Mu/L}$ value when calculated using the two most Li-rich inclusions (0.50, Table S4).

Andalusite. Calculations using 4 C_{Ph} in MH1 yield K_d of 0.13 for P, 0.14 for Zn and 0.07 for Sn. For Li, Be, Sr, Nb and Ba, K_d are ~0.01 and B, Rb, Cs, Ta and W have K_d between 0.01 and 0.001 (Table 5).

Ilmenite. The analysis from a biotite reaction zone has been discarded and the K_d calculations use 12 C_{Ph}, all from Macusani samples. K_d using matrix glasses and MIs differ generally little from each other (Table S4). For B, P and several REE, concentrations in Ilm are mostly below detection (Table S3). Nb and Ta are the two elements the most strongly partitioned in ilmenite. The $K_d(Nb)^{Ilm/L}$ and $K_d(Ta)^{Ilm/L}$ are 91 and 43 respectively (Table 5), similar to in the El Hoyazo enclaves (71 and 46, Acosta-Vigil et al., 2010) but in less good agreement with rhyolitic magmas (106 for Ta, Nash and Crecraft, 1985; 61 for Nb and 74 for Ta, Stimac and Hickmott, 1994; Fig. 13). So, $K_d(Nb)^{Ilm/L}$ / $K_d(Ta)^{Ilm/L}$ is ~2 from our data which implies a small but significant role for Ilm on Nb/Ta fractionation (Stimac and Hickmott, 1994; Stepanov and Hermann, 2013; Stepanov et al., 2014). Another HFSE concentrated in ilmenite is Zr ($K_d(Zr)^{Ilm/L}$ = 1.39) whereas U appears strongly incompatible. W ($K_d(W)^{Ilm/L}$ = 0.44) is moderately less incompatible than Sn ($K_d(Sn)^{Ilm/L}$ = 0.22, Table 5). Mg and the transition metals are strongly incorporated in ilmenite. The $K_d(Mn)^{Ilm/L}$ and $K_d(Zn)^{Ilm/L}$ are both ~22 (Table 5), lower than in the Twin Peaks rhyolite (respectively 115 and 125, Nash and Crecraft, 1985) but in the same range as in the Clear Lake rhyolite and El Hoyazo enclaves (Fig. 13). In contrast, Be and the REE are essentially excluded from ilmenite. La and Gd have low partition coefficients (respectively 0.01 and 0.26, Table 5) above those from the El Hoyazo enclaves (Acosta-Vigil et al., 2010) whereas the mineral separate data for the Twin Peaks rhyolite (Nash and Crecraft, 1985) yield much higher REE K_d (Fig. 13). The large cations (Rb, Cs, Sr) have low to very low K_d (Table 5), in good agreement with the El Hoyazo data (Fig. 13). Pb ($K_d(Pb)^{Ilm/L}$ = 1.18, Table 5) behaves quite differently from the other elements in this group, being also significantly higher than at El Hoyazo (Fig. 13). However, the data are rather dispersed and K_d calculated from the glass inclusion compositions are lower (Table S4).

Tourmaline. Analytical data are available only in glass-free samples which prevents Tur/L partition coefficients to be obtained. Yet, Tur/Biot K_d have been calculated to constrain the partitioning of elements between these two phases. Results using Tur and Biot compositions from MH3 and MH7 (Table S2) show that the two have similar Mg# (Table S1). Tur strongly concentrates the REE relative to Biot (Table S5, Fig. S4; Supplementary material). Be and Sr also prefer the former to the latter phase (Tur/Biot $K_d \geq 1$) whereas the reverse is observed for Li, Mn, Zn, Sn and Pb (K_d = 0.21, 0.29, 0.71, 0.17 and 0.23 respectively, Table S5). Rb, Nb, Cs, Ba, Ta and W have $K_d << 0.01$ (Table S5; Fig. S4) and are strongly depleted in Tur compared to Biot. Therefore, most lithophile elements and rare-metals would concentrate more strongly in peraluminous silicic magmas crystallizing Tur instead of Biot.

Hercynite. The Hc/Biot K_d constrains element partitioning during Biot dehydration melting (Pichavant et al., 1988a). Calculations use Hc and Biot analyzed in biotite reaction zones (Table S2; S3). Four elements, Be, Mn, Zn and U preferentially partition in Hc rather

than Biot (Fig. S4). The Be and U K_d data are quite dispersed and the Mn ($K_d(Mn)^{Hc/Biot} = 1.45$) is much lower than the $K_d(Mn)^{Hc/Biot}$ (157, Table S5). All the other elements have Hc/Biot $K_d \leq 0.1$ (Table S5; Fig. S4). Thus, rare-metals (Nb, Sn, Ta and W) are not sequestered in significant amounts in Hc produced by Biot dehydration melting (Michaud et al., 2021).

5.5. The case of Li partitioning

Among the trace elements considered in this study, Li deserves a separate treatment. For quartz, feldspars and biotite, Li partition coefficients (Table 5; Fig. 11) are generally similar to values for rhyolitic magmas (e.g., Neukampf et al., 2019; Bachmann et al., 2005; Padilla and Gualda, 2016; Dailey et al., 2018; Fig. 11). However, the $K_d(Li)^{Biot/L}$ and the $K_d(Li)^{Mu/L}$ from this study (respectively 3.66 and 1.12, Table 5) are both higher than in experiments (1.7 and 0.8, Icenhower and London, 1995; 0.55 and 0.19, Pichavant et al., 2016) and the $K_d(Li)^{Ilm/L}$ is ~1 order of magnitude above the reference (El Hoyazo, Acosta-Vigil et al., 2010). Li partition coefficients calculated with matrix glasses and the average of glass inclusions are in the same range although in MH1 use of the Li-rich glass inclusions leads to large differences in calculated K_d (Table S4). We also note the systematic K_d variations from one sample to the other. For Qz, Pl, Af, Biot, K_d(Li) in MA85-4 and MA85-7 are well above those in other glass-bearing samples (e.g., $K_d(Li)^{Pl/L}$ = 1.96-2.80 in MA85-7 vs. 0.31-0.41 in MH1). Globally, the $K_d(Li)^{Biot/L}$ vary by ~1 order of magnitude (Table S4), a dispersion comparable to in other silicic magmas (1.2 in the Fish Canyon Tuff, Bachmann et al., 2005, 4.7-10.0 in topaz rhyolites, Dailey et al., 2018). Thus, large uncertainties are associated with the Li K_d, their evaluation (e.g., from Onuma diagrams) being limited by crystal chemical uncertainties. For example, Li coordination in feldspars has been considered alternatively as fourfold (Padilla and Gualda, 2016; Fig. 12) or eightfold (Dohmen and Blundy, 1994; Dailey et al., 2018).

Several factors contribute to this dispersion in Li K_d. Glass Li concentrations vary widely, from 115-687 ppm in matrix glasses, 192-2367 ppm in MIs to 1522-4076 ppm in obsidians. These latter are very H_2O-poor and so extensively degassed (Pichavant et al., 1987), yet they have the highest Li glass concentrations. MIs have Li contents either lower (CR85-2) or higher (MH1) than their corresponding matrix glass (Table 3; 4). The two most Li-rich inclusions in MH1 (enriched in Zn, Zr, La and U and depleted in Be, B, Nb, Cs, Ta and W, Table 4) are melts trapped independently from the other MIs. Clearly, several mechanisms control Li concentrations in melts and glasses (Iveson et al., 2019; Neukampf et al., 2019; Ellis et al., 2022). Concerning phenocrysts, Li in Pl and Af show large dispersions (Fig. 7; 8) and the most elevated Li Qz, Pl, Af, Biot concentrations are found in the same glass-free samples (MH2, MH3, MH7, Table S2, Figs. 5-10). This suggests that sample-specific secondary Li enrichment or redistribution take place in phenocrysts, probably in relation with devitrification of the matrix (see Ellis et al., 2018). For Ilm, post-magmatic alteration and oxidation processes (discussed in Pichavant et al., 1988a) are probably responsible for the observed Li enrichments. We conclude that the Li phenocryst/melt partition coefficients from this study must be considered with caution. As an illustration, the $K_d(Li)^{Qz/L}$ drops from 0.21 (using matrix glasses) to 0.058 (using the two most Li-rich MIs in MH1, Table S4), an evolution similar to in Yellowstone rhyolites (from 0.41-0.45 using matrix glasses to 0.07 using MIs, Neukampf et al., 2019).

6. Implications for crustal magmatism

6.1. Fractionation of Macusani magmas

Results from previous sections provide an internally consistent partitioning dataset for strongly peraluminous silicic magmas. As an application, we model below the geochemical evolution from the matrix glasses and MIs (least fractionated) to the obsidians (most fractionated). The latter have been previously proposed to represent fractionation products from magmas parental to the ash-flow tuffs (Pichavant et al., 1987). The modelling focuses on Macusani samples, those from the separate Picotani field being excluded. Three obsidians (JV1, JV2, JV3), three matrix glasses (MH1, MA85-4, MA85-7) and the two populations of glass inclusions in MH1 are considered. Obsidian CH0 has been excluded because its major element composition differs from the others (Fig. 2; 3; Pichavant et al., 1987). The eight compositions all come from the eastern edge of the Macusani field although stratigraphic relations and ages indicate that the samples are not comagmatic. Rather they represent different snapshots of fractionation along separate lines of descent.

A set of bulk partition coefficients (D) was constructed from the phenocryst/L K_d determined in this study. Melts in the Macusani system are uniformly rhyolitic and magmatic temperatures cover a relatively narrow range (from 650 to 800°C, Pichavant et al., 1988a) and so constant K_d were assumed. Average vol% phenocrysts measured in ash-flow tuffs (Pichavant et al., 1988a) were converted to mass fractions yielding a reference set of D values (case a, Table 6). Other D values obtained by applying an arbitrary -50% correction on the measured vol% Pl, Af, Biot, Af plus Biot and Pl plus Af (cases b to f, Table 6) were tested since, in long-lived large-volume silicic systems, antecryst recycling could artificially increase phenocryst modes (e.g., Jerram and Martin, 2008; Folkes et al., 2011). For some elements (Sr, Ba), the influence of slightly adjusting the K_d in Table 5 was also tested.

Concentrations of trace elements in the liquid were calculated using partial melting and fractional crystallization equations (Allègre et al., 1977; Hanson, 1978; Dailey et al., 2018). The fraction of residual liquid (*f*) was approximated from B concentrations. B has the lowest D in Table 6 (~0.002) and can serve as an indicator of the degree of differentiation. Thus:

$$f = C_0(B)/C_L(B) \quad (2)$$

where subscripts L and 0 refer to residual/final and initial liquids respectively. By replacing *f* by $C_0(B)/C_L(B)$ in the fractional crystallization equation (Allègre et al., 1977), we have, written in logarithmic form for trace element i:

$$LOG(C_L(i)) = LOG\ (C_0(i)) + (D-1)*LOG(C_0(B)) - (D-1)*LOG(C_L(B)) \quad (3)$$

and, for the partial melting equation:

$$LOG(C_L(i)) = LOG\ (C_0(i)) - LOG((D - (C_0(B)/C_L(B))*(D-1)) \quad (4)$$

Trace element evolutions by fractional crystallization (FC, equation (3)) and partial melting (PM, equation (4)) were computed using minimum concentrations among matrix glasses and MIs as initial liquid concentrations (C_0, Table 7).

For the moderately incompatible elements (Rb, Nb, D ~0.5, Table 6), LOG(C_L(i)) increase with LOG(C_L(B)), i.e., with progressive crystallization and decreasing *f* (Fig. 14a). The trends significantly differ between FC and PM, the latter underestimating the obsidian concentrations and, so, FC models are preferable (Fig. 14a). Varying the proportions of fractionating phases and D allows the FC models to be refined and cases e (Rb) and d (Nb) (lowered Af and Biot proportions, Table 6) provide reasonably good fits to the obsidian concentrations (Table 7; Fig. 14a). For the strongly incompatible elements (Sn, Cs, Ta, W, D < 0.15, Table 6), the FC and PM trends almost overlap and LOG(C_L(i)) are lower than in obsidians for the same LOG(C_L(B)) (Fig. 14b). In fact, to be fitted with the initial C_0 values chosen, the data require LOG(C_L(i)) vs. LOG(C_L(B)) slopes > 1, most probably because the samples are not comagmatic. We recall that the slope of equation (3) is (1-D) and so limited to 1 since D is always positive (Allègre et al., 1977). Therefore, the obsidian concentrations can be fitted either by increasing C_0(i) at constant C_0(B), by decreasing C_0(B) at constant C_0(i) or by increasing both C_0(i) and C_0(B). The possibility of C_0(B) being lower than the minimum value (Table 7) was excluded and, so, the obsidian concentrations were fitted by increasing C_0(i) at constant C_0(B). The two sets of calculated C_0(i) (one for JV1/JV2 and the other for JV3) are detailed in Table 7 and the modelling results illustrated in Fig. 14b. The new C_0(i) are significantly higher than the minimum values although, apart from one C_0(Sn), they stay within the range for matrix glasses and MIs (Table 7) and so represent possible incompatible element concentrations for ash-flow tuffs parental melts. We note that increasing C_0 for Rb and Nb, although unnecessary for the modelling, would improve the agreement with the obsidian concentrations (Fig. 14a) suggesting that melts progenitors to the obsidians were consistently more evolved than the least evolved matrix glasses and MIs.

The moderately compatible elements (Sr, Pb, Table 6) show LOG(C_L(i)) decreasing with LOG(C_L(B)). Using the initial set of C_0, the obsidian compositions are again best reproduced with FC. Cases f (Sr) and c (Pb) (Table 6) yield the best fits (Table 7; Fig. 14c). Good fits for Sr were also obtained with case b (Table 6) and adjusting the $K_d(Sr)^{Pl/L}$ from 10.8 to 6.5 (slightly outside the 33% error allowed from Table 5 but within our range of values, Table S4), and by increasing C_0(B) from 799 to 900 ppm, also with case b (Fig. 14c). For Ba, neither FC nor PM models were found to approach the obsidian concentrations whatever the mass fractions. Adjusting $K_d(Ba)^{Af/L}$ from 33 to 21 (again slightly outside the 29% error allowed from Table 5 but within our range of values, Table S4) was necessary to fit the obsidian concentrations with FC in case c (Fig. 14d).

Fractions of residual liquid (*f*) calculated from:

$$f = 100(C(i)/C_0(i))^{1/(D-1)} \quad (5)$$

where C(i) is the concentration in obsidian and D is the value in the best fit model, were used to check the modelling. Concentrations in JV1 and JV2 require degrees of crystallization (100 - *f*) in the same range (54-59%) for the ten elements considered (Table 7). Nb yields a higher value (67%) which is interpreted as an indication for a too low C_0(Nb). JV3 requires 63-67% crystallization to be reproduced (Table 7). Such crystallization ranges are mutually consistent since JV3 is the most evolved. They agree with the residual major element chemistry of obsidians previously inferred from experimental studies (Pichavant et al., 1987; Scaillet et al., 1995; Pichavant, 2022) with again JV3 being the most evolved (highest P_2O_5, F, normative Ab, Table 1). We conclude that trace element modelling globally establishes the possibility to generate the highly evolved obsidian-forming liquids from crystallization-differentiation of melts parental to the ash-flow tuffs.

6.2. Generation of Macusani magmas

Two alternative possibilities were initially considered for the generation of the Macusani Volcanics (Noble et al., 1984): (1) assimilation of metapelitic materials by subaluminous magmas and (2) direct partial melting. The anatectic model (2) was favored as being the most consistent with the mineralogical, geochemical and isotopic signatures of the rocks (Pichavant et al., 1988b). Since the ash-flow tuffs have felsic and strongly homogeneous major element compositions, the possibility that they represent fractionation products from mafic peraluminous magmas was excluded. Therefore, the Macusani Volcanics were interpreted as products of pure crustal anatexis. However, mafic magmas were assigned a key role in the heat supply to the source region (Pichavant et al., 1988b; Cheilletz et al., 1992). Below, this genetic model is revisited and updated.

Mafic magmatism in the Cordillera Oriental and adjacent areas (Kontak et al., 1986; Laubacher et al., 1988; Carlier et al., 1997; Kontak and Clark, 1997; Sandeman et al., 1997; Sandeman and Clark, 2003; 2004; Carlier and Lorand, 2003; Carlier et al., 2005; Carlier and Lorand, 2008) is characterized by potassic to ultrapotassic (K-UK) rocks, including lamproites, minettes and kersantites among other rock types. In the eastern Altiplano, lamproites and minettes have $K_2O/Na_2O > 2$, are strongly reduced and they show very high large ion lithophile element (LILE) and LREE enrichments (Carlier et al., 1997; 2005). Calk-alkaline basalts are also exposed for example in the Cayconi field (Sandeman et al., 1997; Sandeman and Clark, 2004). The mafic magmas have mostly late Oligocene to early Miocene ages (~21-25 Ma, Kontak et al., 1986; Kontak and Clark, 1997; Carlier et al., 1997; 2005; Sandeman et al., 1997; Sandeman and Clark, 2004) and, so, are coeval with the Picotani Group. In contrast, mafic magmatism is practically absent between 5 and 17 Ma (i.e., during eruption of the Quenamari Group). However, eruption of K-UK rocks as young as 0-2 Ma in the magmatic lineament NW of the Cordillera Oriental (Carlier and Lorand, 2008) suggests that mafic activity in fact continued, although unexposed at the surface. The Picotani Group exposes silicic rocks temporally and spatially associated with mafic magmas. Extensive interactions are recorded between the two magma types (Sandeman and Clark, 2004), including the presence of silicic xenocrysts in mafic rocks, specific phenocryst textures and zonations, chemically homogenized hybrid groundmasses, in-between bulk rock compositions and mafic enclaves in silicic volcanics (Kontak et al., 1986; Kontak and Clark, 1997; Carlier et al., 1997; Sandeman and Clark, 2003; Carlier and Lorand, 2008). Subvolcanic mixing between three components, ultrapotassic mafic melts, silicic and calc-alkaline mafic magmas is recorded in the Cayconi field (Sandeman and Clark, 2004) whereas, elsewhere, potassic mafic magmas have a dominant imprint (Sandeman and Clark, 2003).

These observations provide a framework to discuss the origin of the Macusani magmas. No mafic magma erupted contemporaneously with the silicic volcanics in the Quenamari field and mafic microgranular enclaves have not been described in the Macusani ash-flow tuffs. Mineral assemblages lack mafic xenocrysts such as phlogopite or clinopyroxene (Pichavant et al., 1988a). In Picotani Group rocks, the generation of sub-homogeneous hybrids (Kontak et al., 1986; Carlier et al., 1997; Kontak and Clark, 1997; Sandeman and Clark, 2003) suggests that mafic and silicic magmas interacted for a significant time at depth rather than briefly during eruption (Kontak and Clark, 1997; Sandeman and Clark, 2004). However, this does not necessarily mean that the two magmas interacted at the silicic magma source level since mafic

magma recharge is classical in periodically erupted and refilled subvolcanic magma reservoirs (Sparks et al., 1977; Wiebe, 1996; Eichelberger et al., 2000).

The best clues in regard to the Macusani magma source region are provided by the mineralogical data. The early magmatic assemblage includes aluminous phases (biotite, cordierite, tourmaline, sillimanite, hercynite) that strongly suggest pelitic protoliths. This metasedimentary component largely dominates the magma source region. It accounts for the strongly peraluminous nature of the anatectic magmas and is consistent with the mineralogical and isotopic data, in particular the elevated Sr_i and $\delta^{18}O$ values (Pichavant et al., 1987; 1988b). The group II Pl are also part of the early magmatic assemblage and their igneous textures preclude them to represent restites (i.e., metamorphic crystals). Previously, these plagioclases were interpreted to have crystallized from the anatectic melts early in the source region (Pichavant et al., 1988a). This interpretation remains valid as long as An contents are ≤ 30 (Pichavant et al., 2019). However, the group II Pl are commonly more calcic, most having An > 30 and some up to 45 (Pichavant et al., 1988a; Fig. S2; S3; Table S1). Therefore, the initial explanation needs re-examination. One critical observation is that, in mixed rocks from the Picotani Group, plagioclase An contents are in the same range as the group II Pl. An contents in the Minastira granite (a product of mixing between a felsic and a mafic magma) are between 20 and 58 (Kontak and Clark, 1997). In the Cayconi field, the Jama Jama and Pachachaca trachydacites (products of commingling between anatectic and mafic melts) respectively carry An 23-50 and An 22-47 plagioclases (Sandeman and Clark, 2004). Plagioclase microlites in the trachydacitic groundmass of some Puno minettes (lamproites contaminated with peraluminous granites) have An between 35 and 40 (Carlier et al., 1997). Therefore, the group II could represent plagioclases generated during mixing between silicic and mafic magmas.

The trace element data presented in this study corroborate the latter hypothesis. The group II Pl plot off the main trends defined by the group I. They have high Sr and Ba and, for some, high La (Fig. 6; 7). The transition from group I to group II Pl is marked by strong enrichments in Sr, Ba and La (Fig. S3). The group III Pl recognized in this study, with An intermediate between the group I and II, show enrichments in Sr, Ba and La similar to more marked than the group II (Fig. 6; 7). Both the $K_d(Sr)^{Pl/L}$ and the $K_d(Ba)^{Pl/L}$ decrease with An (e.g., Dohmen and Blundy, 2014; Nielsen et al., 2017). However, the $K_d(Sr)^{Pl/L}$ is > 1 until An ~80 (Table 5; Nielsen et al., 2017) whereas the $K_d(Ba)^{Pl/L}$ ranges from ~1 or less at An 10-20 to < 1 above An ~30 (Nielsen et al., 2017). Thus, crystallization of group II and III Pl (An 25-45) should respectively decrease and increase the Sr and Ba concentrations in the residual melt, inconsistent with Sr and Ba both decreasing from group II and III to group I crystals. Therefore, the possibility that the group II and III and the group I Pl are cogenetic, i.e., that the latter crystallized from the residual melt generated by fractionation of the former, can be excluded. Rather, the group II and III Pl must originate from an environment strongly specific chemically given their high Sr, Ba and La concentrations. LILE and LREE enrichments are the signature of Picotani Group mafic rocks and the trace element compositions of group II and III Pl strongly support an origin involving K-UK magmas.

The group II Pl might represent “old” xenocrysts coming from Picotani Group rocks. However, this possibility would be inconsistent with the textural homogeneity of the group II Pl in Macusani samples (cores) and their presence in Quenamari Group silicic volcanics. In addition, enrichments in Sr and Ba are also observed in Af and Biot (Fig. 8; 9). They are associated with low Rb and, so, with compositions that are the least evolved, consistent with the observation of LILE enrichments in early phases such as the group II and III Pl. These elemental enrichments are not accidental. They are most frequently encountered in the same group of samples (MA85-4, MA85-7, MH1), all from the base of the Macusani volcanic

sequence, being also present but much less frequently in the other samples (Fig. 7; 8; 9). Therefore, both the group II and III Pl and the trace element data in Af and Biot record the presence of an exotic LILE- and LREE-rich component during the early magmatic history. Intrusion of K-UK mafic magmas in the source region would supply heat and additional volatiles to promote partial melting. The generation of crustal melts by dehydration-melting and fluid-present reactions (Pichavant et al., 1988b) would be complemented by mixing and hybridization between crustal and K-UK melts. Reactive assimilation of metapelitic source rocks would consume the mafic melts, the group II and III Pl crystallizing during this process. Although volumetrically negligible (modal abundance < 1%), these plagioclases demonstrate that MASH-type processes (Hildreth and Moorbath, 1988) take place in the Macusani magma source region.

The presence of a mafic component in the Macusani magma source region constitutes the main variation from the previous model (Pichavant et al., 1988b). It provides a satisfactory interpretation for the origin of group II Pl and a solution to the heat supply issue. Heat advection driven by intrusion of mantle magmas in the source region is confirmed by the low-velocity zone imaged in the middle crust beneath the Cordillera Oriental (Ma and Clayton, 2014). The new model is also congruous with the style of magmatic activity in the Cordillera Oriental during the late Oligocene to early Miocene. The transition to the 5 to 17 Ma period marked by the near lack of exposed mafic rocks and the shift from mixed mafic-silicic (Picotani Group) to silicic (Quenamari Group) magmatism has been explained by an uplift and thickening of the crust between ca. 23 and 17 Ma (Sandeman and Clark, 2003).

6.3. Broader implications for silicic magma generation

The Macusani Volcanics have been considered as eruptive equivalents of strongly peraluminous granites such as two-mica leucogranites (Pichavant et al., 1988b; Frost et al., 2016) which are granites that probably best fulfill the criteria for an origin by intracrustal melting as summarized by Nabelek (2020) and Moyen et al. (2021). However, despite strong mineralogical and geochemical similarities with plutonic two-mica leucogranites (Pichavant et al., 1988b; Fig. 2), the consequence of protoliths being identical (dominantly metapelites in both cases), the Macusani Volcanics do not fit well in the above intracrustal melting models (Nabelek, 2020; Moyen et al., 2021). The low metamorphic grades in the Cordillera Oriental, volcanic mode of emplacement, high degrees of magma fractionation and thermal regime in the source region are atypical. In contrast, these characteristics are consistent with the key role assigned to mafic magmas as confirmed by the early hybrid phases (the group II and III Pl) identified in this study. They also fit with the mid-crustal depth inferred for the anatectic zone (~20 km, Ma and Clayton, 2014) since garnet is absent in the early mineral assemblage (Pichavant et al., 1988a). Thus, generation of Macusani magmas is, for some aspects, closer to the basalt fractionation than to the intracrustal melting model (Moyen et al., 2021). Moreover, some key magmatic variables bear the signature of the mafic component. The Macusani Volcanics are unusually reduced with fO_2 intermediate between WM and FMQ (Pichavant et al., 1988a), in the same range as Puno minettes which contain ilmenite phenocrysts devoid of Fe^{3+} (as those in this study) and groundmass graphite (Carlier et al., 1997). Similar strongly reducing conditions are also observed in mixed rocks from the Picotani Group (the Revancha dike contains Fe^{3+}- free ilmenite, Sandeman and Clark, 2003). Carbon-bearing, reduced signatures are diagnostic of mantellic sources of lamproites (Carlier et al., 1997) and the

strongly reducing fO_2 reflects in part the influence of the K-UK component in the Macusani magma source region. Similarly, the K-UK rocks of the Cordillera Oriental are F-rich (Carlier et al., 1997), consistent with the elevated F concentrations in Macusani glasses and micas (Table 1; S1) and in Picotani Group biotites (Kontak and Clark, 1997). By shifting mica dehydration melting conditions towards higher temperatures (Pichavant et al., 1988a; Michaud et al., 2021), high F contents promote the generation of more strongly H_2O-undersaturated melts, which favors magma ascent and volcanic emplacement. Elevated F (and Li, B, P) concentrations in the melt lower the solidus and allows crystallization to be pushed down temperature which promotes magma fractionation (Pichavant, 2022). We conclude that several unusual characteristics of the Macusani Volcanics (reduced nature, volcanic emplacement, highly fractionated character) find explanation in specific magma generation mechanisms.

7. Conclusions

Three groups of conclusions emerge from this study. *First*, mineral/melt partition coefficients have been determined by applying the phenocryst/glass approach to the Macusani volcanic suite. The resulting dataset is internally consistent and directly applicable to model fractionation of major mineral phases in strongly peraluminous silicic magmas crystallizing two-mica leucogranites and/or pegmatites. For some phases (Mu, Ilm and And) and elements (in particular Nb, Sn, Ta, W), partition coefficients are presented here for the first time. For Tur and Hc, mineral/biotite partition coefficients are given. Partition coefficients determined in this study have been compared with data from the literature and similarities as well as differences outlined. Partition coefficients for Li are highly variable and still uncertain because several mechanisms influence Li concentrations in melts/glasses as well as in phenocrysts.

Second, fractionation mechanisms in strongly peraluminous silicic magmas have been modelled using the Macusani Volcanics as an example and the origin of the obsidians has been elucidated. The Macusani obsidians record different snapshots of fractionation along separate liquid lines of descent. Trace element modelling shows that crystallization-differentiation of magmas parental to the ash-flow tuffs can generate the evolved liquids represented by the obsidians, consistent with their residual major element composition.

Third, the genetic model proposed for the origin of Macusani magmas has been updated. In addition to the dominant metapelitic component, a mafic component has been identified for the first time in the source region. Mafic magmas (mainly potassic-ultrapotassic and some calk-alkaline) provided heat and volatiles and contributed in small but detectable amounts to magma formation via mixing and hybridization with the anatectic melts. The Macusani Volcanics share several first-order genetic characteristics with plutonic two-mica leucogranites (source rocks, mineral assemblages, major and trace element compositions and isotopic signatures). However, both differ in mode of emplacement, degree of magma fractionation, pressure and temperature regime in the source region and implication of mafic magmas. Melting mechanisms, not only source rocks, has an important influence on the diversity of crustal silicic magmas.

Data availability

Tables of all data presented and discussed in this paper are available through Mendeley Data at https://data.mendeley.com/datasets/c8hww4sw3w/1.

Acknowledgements

This study was supported by the LABEX VOLTAIRE, the ERAMIN project NewOres, the ANR project VARPEG and the SPP 2238 DOME grant no. 1337/49-1. Ida Di Carlo helped with SEM observations and EMPA analyses. M. Harlaux, B. and B. Scaillet are acknowledged for stimulating discussions and reviews of early versions and B. Schmidt and J. F. Stebbins for sharing their knowledge about B speciation. The paper benefited from reviews by Q.-Q. Zhang, A. A. Iveson and an anonymous reviewer, as well as from editorial work by Z. Zajacz.

Appendix A. Supplementary material

Supplementary tables include details of partition coefficient calculations for the phenocryst/L (Table S4) and for mineral/biotite (Table S5). Supplementary figures (and associated captions) include SEM views of Qz (Fig. S1) and Pl phenocrysts (Fig. S2; S3). Major and trace element variations across the transition from group I to group II Pl are documented in Fig. S2 and S3. Partition coefficients between tourmaline, hercynite and biotite are illustrated in Fig. S4. Supplementary material to this article can be found online at https://doi.org/10.1016/j.gca.[ ].

References

Acosta-Vigil, A., Buick, I., Hermann, J., Cesare, B., Rubatto, D., London, D., Morgan, G.B. VI, 2010. Mechanisms of crustal anatexis: a geochemical study of partially melted metapelitic enclaves and host dacite, SE Spain. J. Petrol. 51, 785-821.

Allègre, C.-J., Treuil, M., Minster, J.-F., Minster, B., Albarède, F., 1977. Systematic use of trace element in igneous process. Part I: Fractional crystallization processes in volcanic suites. Contrib. Mineral. Petrol. 60, 57-75.

Bachmann, O., Dungan, M.A., Bussy, F., 2005. Insights into shallow magmatic processes in large silicic magma bodies: the trace element record in the Fish Canyon magma body, Colorado. Contrib. Mineral. Petrol. 149, 338-349.

Ballouard, C., Boulvais, Ph., Poujol, M., Gapais, D., Yamato, Ph., Tartèse, R., Cuney, M., 2015. Tectonic record, magmatic history and hydrothermal alteration in the Hercynian Guérande leucogranite, Armorican Massif, France. Lithos 220-223, 1-22.

Ballouard, C., Elburg, M., Tappe, S., Reinkeb, C., Ueckermann, H., Doggart, S., 2020. Magmatic-hydrothermal evolution of rare-metal pegmatites from the Mesoproterozoic Orange River pegmatite belt (Namaqualand, South Africa). Ore Geol. Rev. 116, 103252.

Bindeman, I.N., Davis, A.M., 2000. Trace element partitioning between plagioclase and melt: Investigation of dopant influence on partition behavior. Geochim. Comochim. Acta, 64, 2863–2878.

Breiter, K., Fryda, J., Seltmann, R., Thomas, R., 1997. Mineralogical evidence for two magmatic stages in the evolution of an extremely fractionated P-rich rare-metal granite: the Podlesı stock, Krusne Hory, Czech Republic. J. Petrol. 38, 1723-1739.

Carlier, G., Lorand, J.-P., 2003. Petrogenesis of a zirconolite-bearing Mediterranean-type lamproite from the Peruvian Altiplano (Andean Cordillera). Lithos 69, 15-35.

Carlier, G., Lorand, J.-P., 2008. Zr-rich accessory minerals (titanite, perrierite, zirconolite, baddeleyite) record strong oxidation associated with magma mixing in the south Peruvian potassic province. Lithos 104, 54-70.

Carlier, G., Lorand, J.-P., Audebaud, E., Kienast, J.-R., 1997. Petrology of an unusual orthopyroxene-bearing minette suite from southeastern Peru, Eastern Andean Cordillera: Al-rich lamproites contaminated by peraluminous granites. J. Volcanol. Geotherm. Res. 75, 59-87.

Carlier, G., Lorand, J.-P., Liégeois, J.-P., Fornari, M., Soler, P., Carlotto, V., Cardenas, J., 2005. Potassic-ultrapotassic mafic rocks delineate two lithospheric mantle blocks beneath the southern Peruvian Altiplano. Geology 33, 601-604.

Cerny, P., Masau, M., Goad, B.E., Ferreira, K., 2005. The Greer Lake leucogranite, Manitoba, and the origin of lepidolite-subtype granitic pegmatites. Lithos 80, 305-321.

Cesare, B., Cruciani, G., Russo, U., 2003. Hydrogen deficiency in Ti-rich biotite from anatectic metapelites (El Hoyazo, SE Spain): Crystal-chemical aspects and implications for high-temperature petrogenesis. Am. Mineral., 88, 583–595.

Charoy, B., Noronha, F., 1996. Multistage growth of a rare-element, volatile-rich microgranite at Argemela (Portugal). J. Petrol. 37, 73-94.

Cheilletz, A., Clark, A.H., Farrar, E., Arroyo Pauca, G., Pichavant, M., Sandeman, H.A., 1992. Volcano-stratigraphy and $^{40}Ar/^{39}Ar$ geochronology of the Macusani ignimbrite field: monitor of the Miocene geodynamic evolution of the Andes of southeast Peru. Tectonophysics 205, 307-327.

Christiansen, E.H., Bikun, J.V., Sheridan, M.F., Burt, D.M., 1984. Geochemical evolution of topaz rhyolites from the Thomas Range and Spor Mountain, Utah. Am. Mineral. 69, 223-236.

Christiansen, E.H., Sheridan, M.F., Burt, D.M., 1986. The geology and geochemistry of Cenozoic topaz rhyolite from the western United States. Geological Society of America Special Paper 205, 1–82.

Clarke, D. B., 1981. The mineralogy of peraluminous granites: A review. Can. Mineral., 19, 3–17.

Congdon, R.D., Nash, W.P., 1991. Eruptive pegmatite magma: rhyolite of the Honeycomb Hills, Utah. Am. Mineral 76, 1261-1278.

Cuney, M., 2014. Felsic magmatism and uranium deposits. Bull. Soc. Geol. France 185, 75-92.

Cuney, M., Barbey, P., 2014. Uranium, rare-metals, and granulite-facies metamorphism. Geosci. Front. 5, 729–745.

Cuney, M., Marignac, C., Weisbrod, A., 1992. The Beauvoir topaz-lepidolite albite granite (Massif Central, France): The disseminated magmatic Sn-Li-Ta-Nb-Be mineralization. Econ. Geol. 87, 1766-1794.

Dailey, S.R., Christiansen, E.H., Dorais, M.J., Kowallis, B.J., Fernandez, D.P., Johnson, D.M., 2018. Origin of the fluorine- and beryllium-rich rhyolites of the Spor Mountain Formation, Western Utah. Am. Mineral 103, 1228-1252.

Debon, F., Le Fort, P., 1983. A chemical-mineralogical classification of common plutonic rocks and associations. Trans. R. Soc. Edinburgh: Earth Sci. 73, 135-149.

Dohmen, R., Blundy, J., 1994. A predictive thermodynamic model for element partitioning between plagioclase and melt as a function of pressure, temperature and composition. Am. J. Sci. 314, 1319-1372.

Eichelberger, J. C., Chertkoff, D. G., Dreher, S. T., Nye, C. J., 2000. Magmas in collision: rethinking chemical zonation in silicic magmas. Geology 28, 603-606.

Ellis, B.S., Szymanowski, D., Magna, T., Neukampf, J., Dohmen, R., Bachmann, O., Ulmer, P., Guillong, M., 2018. Post-eruptive mobility of lithium in volcanic rocks. Nature Comm. 9, 3228.

Ellis, B.S., Szymanowski, D., Harris, C., Tollan, P.M.E., Neukampf, J., Guillong, M., Cortes-Calderon, E.A., Bachmann, O., 2022. Evaluating the potential of rhyolitic glass as a lithium source for brine deposits. Econ. Geol. 117, 91-105.

Evensen, J.M., London, D., 2002. Experimental silicate mineral/melt partition coefficients for beryllium and the crustal Be cycle from migmatite to pegmatite. Geochim. Cosmochim. Acta 66, 2239–2265.

Fabre, C., Maurice, S., Cousin, A., Wiens, R.C., Forni, O., Sautter, V., Guillaume, D., 2011. Onboard calibration igneous targets for the Mars Science Laboratory Curiosity rover and the Chemistry Camera laser induced breakdown spectroscopy instrument. Spectrochimica Acta Part B 66, 280–289.

Folkes, C.B., de Silva, S., Schmitt, A.K., Cas, R.A.F., 2011. A reconnaissance of U-Pb zircon ages in the Cerro Galán system, NW Argentina: Prolonged magma residence, crystal recycling, and crustal assimilation. J. Volcanol. Geotherm. Res., 206, 136–147.

Frost, C.D., Frost, B.R., Beard, J.S., 2016. On silica-rich granitoids and their eruptive equivalents. Am. Mineral. 101, 1268-1284.

Gao, M., Xiong, X., Huang, F., Wang, J., Wei, C., 2023. Key factors controlling biotite–silicate melt Nb and Ta partitioning: Implications for Nb−Ta enrichment and fractionation in granites. J. Geophys. Res. Solid Earth, 128, e2022JB025889. https://doi.org/10.1029/2022JB025889.

Griffin, W.L., 2008. GLITTER: data reduction software for laser ablation ICP-MS, in: Sylvester, P. (Ed.) Laser ablation ICP-MS in the earth sciences: current practices and outstanding issues. Mineralogical Association of Canada, Vancouver, pp 308–311.

Hanson, G., 1978. The application of trace elements to the petrogenesis of igneous rocks of granitic composition. Earth Planet. Sci. Lett. 38, 26-43.

Hildreth, W., Moorbath, S., 1988. Crustal contribution to arc magmatism in the Andes of Central Chile. Contrib. Mineral. Petrol. 98, 455–489.

Hulsbosch, N., 2019. Nb-Ta-Sn-W distribution in granite-related ore systems: fractionation mechanisms and examples from the Karagwe-Ankole belt of Central Africa, in: Decree, S., Robb, L. (Eds.), Ore Deposits, Origin, Exploitation. and Exploitation. American Geophysical Union, Washington, pp. 75-107.

Icenhower, J., London, D., 1995. An experimental study of element partitioning among biotite, muscovite and coexisting peraluminous silicic melt at 200 MPa (H_2O). Am. Mineral. 80, 1229–1251.

Icenhower, J., London, D., 1996. Experimental partitioning of Rb, Cs, Sr, and Ba between alkali feldspar and peraluminous melt. Am. Mineral. 81, 719-734.

Icenhower, J., London, D., 1997. Partitioning of fluorine and chlorine between biotite and granitic melt: experimental calibration at 200 MPa H_2O. Contrib. Mineral. Petrol. 127, 17-29.

Iveson, A.A., Webster, J.D., Rowe, M.C., Neill, O.K., 2019. Fluid–melt trace-element partitioning behaviour between evolved melts and aqueous fluids: Experimental constraints on the magmatic-hydrothermal transport of metals. Chem. Geol. 516, 18–41.

Jenner, F.E., Arevalo, R.D.Jr., 2016. Major and trace element analysis of natural and experimental igneous systems using LA–ICP–MS. Elements 12, 311-316.

Jerram, D.A., Martin, V.M., 2008; Understanding crystal populations and their significance through the magma plumbing system, in: Annen, C., Zellmer, G. F. (Eds), Dynamics of Crustal Magma Transfer, Storage and Differentiation. Geological Society, London, Special Publications, 304, pp. 133–148.

Jochum, K.P., Nohl, U., Herwig, K., Lammel, E., Stoll, B., Hofmann, A.W., 2005. GeoReM: a new geochemical database for reference materials and isotopic standards. Geostand. Geoanal. Res. 29, 333-338.

Kontak, D.J., Clark, A.H., 1997. The Minastira peraluminous granite, Puno, southeastern Peru: a quenched, hypabyssal intrusion recording magma commingling and mixing. Mineral. Mag. 61, 743-764.

Kontak, D.J., Clark, A.H., Farrar, E., Pearce, T.E., Strong, D.F., Baadsgaard, H., 1986. Petrogenesis of a Neogene shoshonite suite, Cerro Moromoroni, Puno, Southeastern Peru. Can. Mineral. 24, 117-135.

Korges, M., Weis, Ph., Lüders, V., Laurent, O., 2018. Depressurization and boiling of a single magmatic fluid as a mechanism for tin-tungsten deposit formation. Geology 46, 75-78.

Kovalenko, V.I., Kovalenko, N.I., 1976. Ongonites (Topaz-Bearing Quartz Keratophyres) Subvolcanic Analogues of Rare-Metal Li-F Granites. Nauka, Moscow.

Laubaucher, G. 1978. Géologie de la Cordillère Orientale et de l'Altiplano au Nord et au Nord-Ouest du Lac Titicaca. ORSTOM Travaux et Documents, Paris.

Laubacher, G., Sebrier, M., Fornari, M., Carlier, B., 1988. Oligocene and Miocene continental sedimentation, tectonics, and S-type magmatism in the southeastern Andes of Peru (Crucero Basin): Geodynamic implications. J. South Am. Earth Sci. 1, 225-238.

Li, V.V., 2016. The Uranium Mineralization of the Macusani District, Southeast Peru: Mineralogy, Geochemistry, Geochronology and Ore-Genetic Model. PhD Thesis, Queen's University, Kingston.

Linnen, R.L., 1998. The solubility of Nb-Ta-Zr-Hf-W in granitic melts with Li and Li + F: constraints for mineralization in rare-metal granites and pegmatites. Econ. Geol. 93, 1913-1925.

Linnen, R.L., Cuney, M., 2005. Granite-related rare-element deposits and experimental constraints on Ta-Nb-W-Sn-Zr-Hf mineralization, in: Linnen, R.L., Samson, I.M. (Eds.), Rare-element geochemistry and mineral deposits. Geological Association of Canada, Ottawa, pp. 45-68.

Liu, C., Wang, R.C., Wu, F.Y., Xie, L., Liu, X.C., Li, X.K., Yang, L., Li, X.J., 2020. Spodumene pegmatites from the Pusila pluton in the higher Himalaya, South Tibet: Lithium mineralization in a highly fractionated leucogranite batholith. Lithos 358-359, 105421.

London, D., 2015. Reply to Thomas and Davidson on "A petrologic assessment of internal zonation in granitic pegmatites" (London, 2014a). Lithos 212–215, 469–484.

London, D., 2008. Pegmatites. Mineralogical Association of Canada, Ottawa.

Ma, Y., Clayton, R. W., 2014. The crust and uppermost mantle structure of Southern Peru from ambient noise and earthquake surface wave analysis. Earth Planet. Sci. Lett. 395, 61–70.

May, T.W., Wiedmeyer, R.H., 1998. A table of polyatomic interferences in ICP-MS. At. Spectroscopy, 19, 150-155.

Müller, M., Koch-Müller, A., 2009. Hydrogen speciation and trace element contents of igneous, hydrothermal and metamorphic quartz from Norway. Mineral. Mag., 73, 569–583

Müller, A., Romer, R., Pedersen, R.B., 2017. The Sveconorwegian pegmatite province — thousands of pegmatites without parental granites. Can. Mineral. 55, 283–315.

Michaud, J.A.-S., Pichavant, M., 2020. Magmatic fractionation and the magmatic-hydrothermal transition in rare-metal granites: evidence from Argemela (Central Portugal). Geochim. Cosmochim. Acta 289, 130-157.

Michaud, J.A.-S., Pichavant, M., Villaros, A., 2021. Rare elements enrichment in crustal peraluminous magmas: insights from partial melting experiments. Contrib. Mineral. Petrol. 176, 96.

Moyen, J.-F., Janousek, V., Laurent, O., Bachmann, O., Jacob, J.-B., Farina, F., Fiannacca, P., Villaros, A., 2021. Crustal melting vs. fractionation of basaltic magmas: Part 1, granites and paradigms. Lithos 402-403, 106291.

Nabelek, P.I., 2020. Petrogenesis of leucogranites in collisional orogens, in: Janousek, V., Bonin, B., Collins, W. J., Farina, F., Bowden, P. (Eds), Post-Archean Granitic Rocks: Petrogenetic Processes and Tectonic Environments. Geological Society, London, Special Publications, 491, pp. 179–207.

Nabelek, P.I., Russ-Nabelek, C., Denison, J.R., 1992a. The generation and crystallization conditions of the Proterozoic Harney Peak Leucogranite, Black Hills, South Dakota, USA: Petrologic and geochemical constraints. Contrib. Mineral. Petrol. 110, 173-191.

Nabelek, P.I., Russ-Nabelek, C., Haeussler, G.T., 1992b. Stable isotope evidence for the petrogenesis and fluid evolution in the Proterozoic Harney Peak leucogranite, Black Hills, South Dakota. Geochim. Cosmochim. Acta 56, 403-417.

Nash, W.P., Crecraft, H.R., 1985. Partition coefficients for trace elements in silicic magmas. Geochim. Cosmochim. Acta 49, 2309-2322.

Neukampf, J., Ellis, B.S., Magna, T., Laurent, O., Bachmann, O., 2019. Partitioning and isotopic fractionation of lithium in mineral phases of hot, dry rhyolites: The case of the Mesa Falls Tuff, Yellowstone. Chem. Geol. 506, 175-186.

Nielsen, R.L., Ustunisik, G., Weinsteiger, A.B., Tepley, F.J. III, Johnston, A.D., Kent, A.J.R., 2017. Trace element partitioning between plagioclase and melt: An investigation of the impact of experimental and analytical procedures. Geochem. Geophys. Geosyst., 18, 3359–3384.

Noble, D.C., Vogel, T.A., Peterson, P.S., Landis, G.P., Grant, N.K., Jezek, P.A., McKee, E.H., 1984. Rare-element-enriched, S-type ash-flow tuffs containing phenocrysts of muscovite, andalusite, and sillimanite, southeastern Peru. Geology 12, 35-39.

Onuma, N., Higuchi, H., Wakita, H., Nagasawa, H., (1968). Trace element partitioning between two pyroxenes and the host lava. Earth Planet. Sci. Lett., 5, 47–51.

Padilla, A.J., Gualda, G.A.R., 2016. Crystal-melt elemental partitioning in silicic magmatic systems: an example from the Peach Spring Tuff high-silica rhyolite, Southwest USA. Chem. Geol. 440, 326-344.

Partington, G.A., McNaughton, N.J, Williams, I.S., 1995. A review of the geology, mineralization and geochronology of the Greenbushes Pegmatite, Western Australia. Econ. Geol 90, 616-635.

Pearce, N.J.G., Perkins, W.T., Westgate, J.A., Gorton, M.P., Jackson, S.E., Neal, C.R., Chenery, S.P., 1997. A compilation of new and published major and trace element data for NIST SRM 610 and NIST SRM 612 glass reference materials. Geostandards Newsletter 21, 115-144.

Pichavant, M., 2022. Experimental crystallization of the Beauvoir granite as a model for the evolution of Variscan rare-metal magmas. J. Petrol. 63, egac120.

Pichavant, M., Valencia Herrera, J., Boulmier, S., Briqueu, L., Joron, J.-L., Juteau, M., Michard, A., Sheppard, S.M.F., Treuil, M., Vernet, M., 1987. The Macusani glasses, SE Peru: evidence of chemical fractionation in peraluminous magmas, in: Mysen, B.O. (Ed.), Magmatic Processes: Physicochemical Principles. The Geochemical Society, University Park, pp. 359–373.

Pichavant, M., Kontak, D., J., Valencia Herrera, J., Clark, A.H., 1988a. The Miocene-Pliocene Macusani Volcanics, I. Mineralogy and magmatic evolution of a two-mica aluminosilicate-bearing ignimbrite suite. Contrib. Mineral. Petrol. 100, 300-324.

Pichavant, M., Kontak, D., J., Briqueu, L., Valencia Herrera, J., Clark, A.H., 1988b. The Miocene-Pliocene Macusani Volcanics, II. Geochemistry and origin of a felsic peraluminous magma. Contrib. Mineral. Petrol. 100, 325-338.

Pichavant, M., Villaros, A., Deveaud, S., Scaillet, B., Lahlafi, M., 2016. The influence of redox state on mica crystallization in leucogranitic and pegmatitic liquids. Can. Mineral. 54, 559-581.

Pichavant, M., Weber, C., Villaros, A., 2019. Effect of anorthite on granite phase relations: experimental data and models. C. R. Geosciences 351, 540-550.

Poupeau, G., Sabil, N., Villa, I.M., Bigazzi, G., Vatin-Perignon, N., Flores, P., Pereyra, P., Salas, G., Arroyo, G., 1992. Fission-track and K-Ar ages of “macusanite” obsidian glasses (SE Peru): geodynamic implications. Tectonophysics 205, 285-305.

Poupeau, G., Labrin, E., Sabil, N., Bigazzi, G., Arroyo, G., Vatin-Perignon, N., 1993. Fission-track dating of 15 macusanite glass pebbles from the Macusani volcanic field (SE Peru). Nucl Tracks Radiat. Meas. 21, 499-506.

Prowatke, S., Klemme, S., 2006. Trace element partitioning between apatite and silicate melts. Geochim. Cosmochim. Acta 70, 4513-4527.

Raimbault, L., Cuney, M., Azencott, C., Duthou, J.-L., Joron, J.-L., 1995. Geochemical evidence for a multistage magmatic genesis of Ta-Sn-Li mineralization in the granite at Beauvoir, French Massif Central. Econ. Geol. 90, 548-576.

Raimbault, L., Burnol, L., 1998. The Richemont rhyolite dyke, Massif Central, France: a subvolcanic equivalent of rare-metal granites. Can Mineral 36, 265-282.

Ren, M., 2004. Partitioning of Sr, Ba, Rb, Y and LREE between alkali feldspar and peraluminous silicic magma. Am. Mineral., 89, 1290-1303.

Ren, M., Parker, D.F., White, J.C., 2003. Partitioning of Sr, Ba, Rb, Y, and LREE between plagioclase and peraluminous silicic magma. Am. Mineral. 88, 1091-1103.

Roda-Robles, E., Villaseca, C., Pesquera, A., Gil-Crespo, P.P., Vieira, R., Lima, A., Garate-Olave, I., 2018. Petrogenetic relationships between Variscan granitoids and Li-(F-P)-rich aplite-pegmatites in the Central Iberian Zone: geological and geochemical constraints and implications for other regions from the European Variscides. Ore Geol. Rev. 95, 408-430.

Romer, R.L., Pichavant, M., 2021. Rare-metal granites and pegmatites, in: Alderton, D., Elias, S.A. (Eds.), Encyclopedia of Geology 2nd, Academic Press, pp. 840-846.

Sandeman, H.A., Clark, A.H., 2003. Glass-rich, cordierite-biotite rhyodacite, Valle Ninahuisa, Puno, SE Peru: petrological evidence for hybridization of "Lachlan S-type" and potassic mafic magmas. J. Petrol. 44, 355-385.

Sandeman, H.A., Clark, A.H., 2004. Commingling and mixing of S-type peraluminous, ultrapotassic and basaltic magmas in the Cayconi volcanic field, Cordillera de Carabaya, SE Peru. Lithos 73, 187-213.

Sandeman, H.A., Clark, A.H., Farrar, E., Arroyo Pauca, G., 1996. A critical appraisal of the Cayconi Formation, Crucero Basin, southeastern Peru. J. South Am. Earth Sci. 9, 381-392.

Sandeman, H.A., Clark, A.H., Farrar, E., Arroyo Pauca, G., 1997. Lithostratigraphy, petrology and ^{40}Ar-^{39}Ar geochronology of the Crucero Supergroup, Puno Department, SE Peru. J. South Am. Earth Sci. 10, 223-245.

Scaillet, B., Pichavant, M., Roux, J., 1995. Experimental crystallization of leucogranite magmas. J. Petrol. 36, 663-705.

Simpson, D.R., 1977. Aluminum phosphate variants of feldspar. Am. Mineral., 62, 1351-1355.

Sparks, S.R.J., Sigurdsson, H., Wilson, L., 1977. Magma mixing: a mechanism for triggering acid explosive eruptions. Nature 267, 315-318.

Stemprok, M., 2016. Drill hole CS-1 penetrating the Cínovec/Zinnwald granite cupola (Czech Republic): a A-type granite with important hydrothermal mineralization. J. Geosci. 61, 395-423.

Stepanov, A.S., Hermann, J., 2013. Fractionation of Nb and Ta by biotite and phengite: Implications for the "missing Nb paradox". Geology 41, 303-306.

Stepanov, A., Mavrogenes, J.A., Meffre, S., Davidson, P., 2014. The key role of mica during igneous concentration of tantalum. Contrib. Mineral. Petrol. 167, 1009.

Stewart, D.B., 1978. Petrogenesis of lithium-rich pegmatites. Am. Mineral. 63, 970-980.

Stilling, A., Cerny, P., Vanstone, P.J., 2006. The Tanco pegmatite at Bernic Lake, Manitoba. XVI. Zonal and bulk compositions and their petrogenetic significance. Can. Mineral. 44, 599-623.

Stimac, J., Hickmott, D., 1994. Trace-element partition coefficients for ilmenite, orthopyroxene and pyrrhotite in rhyolite determined by micro-PIXE analysis. Chem. Geol. 117, 313-330.

Stix, J., Gorton, M.P., 1990. Variations in trace element partition coefficients in sanidine in the Cerro Toledo Rhyolite, Jemez Mountains, New Mexico: Effects of composition, temperature, and volatiles. Geochim. Cosmochim. Acta 54, 2697-2708.

Thomas, R., 2013. Practical Guide to ICP-MS, A Tutorial for Beginners, Third Edition, eBook, https://doi.org/10.1201/b14923.

Thomas, R., Davidson, P., 2012. Water in granite and pegmatite-forming melts. Ore Geol. Rev. 46, 32-46.

Villaros, A., Pichavant, M., 2019. Mica-liquid trace elements partitioning and the granite-pegmatite connection: The St-Sylvestre complex (Western French Massif Central). Chem. Geol. 528, 119265.

Villaseca, C., Barbero, L., Herreros, V., 1998. A re-examination of the typology of peraluminous granite types in intracontinental orogenic belts. Trans. R. Soc. Edinburgh: Earth Sci. 89, 113-119.

Waters, D.J., Charnley, N.R., 2002. Local equilibrium in polymetamorphic gneiss and the titanium substitution in biotite. Am. Mineral., 87, 383–396.

Were, P., Keppler, H., 2021. Trace element fractionation between biotite, allanite, and granitic melt. Contrib. Mineral. Petrol., 176:74 https://doi.org/10.1007/s00410-021-01831-3.

Wiebe, R.A. (1996). Mafic-silicic layered intrusions: the role of basaltic injections on magmatic processes and the evolution of silicic magma chambers. Trans. R. Soc. Edinburgh: Earth Sci. 87, 233-242.

Figure captions

Fig. 1. SEM BSE images of studied samples showing glass textures. (a) General view of sample MH1 (Quenamari field) showing a large biotite phenocryst (Biot) partly engulfed in a pumice clast with glassy filaments right and below the crystal, and broken quartz (Qz), sanidine (Af) and plagioclase (Pl) phenocrysts. The small light grey crystal left of biotite is apatite and the two crystals appearing in white are ilmenites. (b) Detail of glass filaments (Gl) in pumice clast, sample MH1. Notice the homogeneous grey color of the glass in BSE mode and the lack of microlites. (c) Glassy groundmass (Gl) ranging from dense bubble-free to locally bubble-rich, sample CR85-1 (Picotani field). A large biotite (Biot) phenocryst appears at the left. (d) Glass inclusion (Gl) exposed at the surface of a quartz (Qz) phenocryst, sample MH1.

Fig. 2. Major element compositions of glasses and ash-flow tuffs plotted in the A'-B' diagram (A' = 1000*(Al-(Na+K+2Ca) at., B' = 1000*(Fe+Mg+Ti) at., Debon and Le Fort, 1983; Villaseca et al., 1998; Cuney, 2014). Glass compositions from Table 1. Ash-flow tuff compositions from Pichavant et al. (1988b) with black symbols for the Quenamari field and the purple symbol for the Picotani field. The obsidian symbols are labelled with their sample

number to emphasize the less peraluminous character of CH0 relative to JV2 and JV3. The cross shows the average errors on A' and B' for glasses calculated by propagating the EMPA analytical errors (see text). For comparison, compositions of rare-metal granites (Beauvoir, Raimbault et al., 1995; Argemela, Charoy and Noronha, 1996; Michaud and Pichavant, 2020) and peraluminous two-mica leucogranites (Ballouard et al., 2015; Villaros and Pichavant, 2019) are shown as (+) and (x) respectively and compositions of the Richemont rhyolite (Raimbault and Burnol, 1998) as (Δ).

Fig. 3. Trace element Rb variation diagrams for matrix glasses (matrix gl.) and obsidians. Data for obsidians are from Table 2 and for matrix glasses from Table 3. Error bars are individual standard deviations (s.d., Table 2; 3). When absent, error bars are smaller than symbols.

Fig. 4. Comparison between trace element concentrations in matrix glasses (matrix gl.) and glass inclusions (MIs) in samples MH1 and CR85-2. Average data for matrix glasses and glass inclusions are from Table 3 and 4 respectively. Error bars are individual standard deviations (s.d., Table 3) for matrix glasses and average standard deviations (s.d., Table 4) for glass inclusions. When absent, error bars are smaller than symbols.

Fig. 5. Al and Li concentrations in quartz. Data from Table S2. The solid diamonds refer to the glass-bearing and the crosses to the glass-free samples. Li = Al on an atomic basis is represented by the 1:1 dashed line. Relative errors calculated with 1 σ uncertainties from the Glitter software (Table S2) are 4.0% (Li) and 4.3% (Al). Error bars are smaller to slightly larger than symbols.

Fig. 6. Sr (a) and Ba (b) concentrations in plagioclases plotted as a function of their anorthite content (An). Data from Table S2. The solid diamonds refer to the glass-bearing and the other symbols (crosses and circle) to the glass-free samples. Compositional domains corresponding to the group I, II and III plagioclases are indicated (see also text). Relative errors calculated with 1 σ uncertainties from the Glitter software (Table S2) are 4.4% (Sr) and 5.4% (Ba). Error bars for the group I and group II compositions are smaller than symbols. For the two group III data points above 1000 ppm Sr and 500 ppm Ba, error bars are up to 1.5 to 2 times larger than symbols.

Fig. 7. P (a), Eu (b), Pb (c) and Li (d) concentrations in plagioclases plotted as a function of Sr. Data from Table S2. The solid diamonds refer to the glass-bearing and the other symbols (crosses and circle) to the glass-free samples. Relative errors calculated with 1 σ uncertainties from the Glitter software (Table S2) are 4.4% (Sr), 6.2% (P), 6.0% (Eu), 4.5% (Pb) and 3.5% (Li). Error bars for Sr concentrations < 750 ppm are smaller than symbols.

Fig. 8. Sr (a), Eu (b), P (c) and Li (d) concentrations in sanidines plotted as a function of Rb. Data from Table S2. The solid diamonds refer to the glass-bearing and the other symbols (crosses and circle) to the glass-free samples. Arrows indicate the four specific data points discussed in text. Relative errors calculated with 1 σ uncertainties from the Glitter software (Table S2) are 3.9% (Rb), 4.2% (Sr), 6.1% (P), 5.1% (Eu), 3.5% (Li). For Sr, P, Eu, Li, error bars are smaller than symbols. For Rb, error bars are smaller than symbols at low concentrations (~600 ppm) and ~2 times larger than symbols at high Rb concentrations (~900 ppm).

Fig. 9. Mg# (a), Ta (b), Li (c) and Ba (d) concentrations in biotites plotted as a function of Rb. Data from Table S2. For the other elements, see figures associated with Table S2. The solid diamonds refer to the glass-bearing and the other symbols (crosses and circles) to the glass-free samples. Relative errors calculated with 1 σ uncertainties from the Glitter software (Table S2) are 3.6% (Rb), 3.4% (Li, Ba, Ta). Error bars are smaller than symbols except for Li at high concentrations (~4500 ppm) where they are slightly higher than symbols.

Fig. 10. Li (a) and W (b) concentrations in muscovites plotted as a function of Rb. Data from Table S2. For the other elements, see figures associated with Table S2. The solid diamonds refer to the glass-bearing and the other symbols (crosses) to the glass-free samples. Relative errors calculated with 1 σ uncertainties from the Glitter software (Table S2) are 3.9% (Rb), 3.7% (Li), 3.5% (W). Error bars are smaller than symbols.

Fig. 11. Partition coefficients between quartz and melt, plagioclase and melt, sanidine and melt and biotite and melt determined in this study. Median values appear as red squares (Table 5) and minimum and maximum values as small horizontal bars (Table S4). Partitioning data for topaz rhyolites (Dailey et al., 2018, blue circles), Fish Canyon Tuff (Bachmann et al., 2005, green circles) and Peach Spring Tuff (Padilla and Gualda, 2016, black circles) are shown for reference.

Fig. 12. Ln(K_d) vs. ionic radius plots (Onuma diagrams) for plagioclase, sanidine, biotite and muscovite. Partition coefficients from Table 5 and ionic radii (for appropriate valence and coordination number) from http://abulafia.mt.ic.ac.uk/shannon/ptable.php. For Sn^{2+}, ionic radii estimated from Dailey et al. (2018). Curves are hand-made regressions. See text.

Fig. 13. Partition coefficients between muscovite and melt and ilmenite and melt determined in this study. Median values appear as red squares (Table 5) and minimum and maximum values as small horizontal bars (Table S4). For muscovite, partitioning data for the Richemont rhyolite (Raimbault and Burnol, 1998, blue circles) are shown for reference. For ilmenite, partitioning data for the El Hoyazo enclaves (Acosta-Vigil et al., 2010), Twin Peaks rhyolite (Nash and Crecraft, 1985) and Clear Lake rhyolite (Stimac and Hickmott, 1994) are shown for reference.

Fig. 14. Results of geochemical modelling. Logarithms of Rb, Ta, Sr, Ba concentrations plotted as a function of the logarithm of B concentrations for obsidians JV1, JV2, JV3, matrix glasses (Macusani samples MH1, MA85-4, MA85-7) and MIs (MH1). Analytical data from Tables 2-4. Results of fractional crystallization (FC) and partial melting (PM) are shown respectively as + and solid lines and as x and dashed curves, with calculations made for LOG(B) increments of 0.05. C_0: initial trace element concentration (Table 7). (a) Calculations performed with D calculated from cases a, b, e (Table 6). (b) Calculations all performed with D calculated from case a (Table 6). Increasing C_0 is necessary to fit the obsidian concentrations. See Table 7 and text. (c). Calculations performed with D calculated from cases a, b, d, f (Table 6). Note that PM calculations overlap for the a and d cases. (d). Calculations performed with D calculated from cases a, b, c, (Table 6); D* indicates calculations performed with D adjusted by lowering $K_d(Ba)^{Af/L}$ and phase proportions in case c as explained in text.

Table 1. Major element compositions of glasses

Sample	MH1		MH1		MA85-4		MA85-4		MA85-7		CR85-1
Type	matrix		MI		matrix		MI		matrix		matrix
n	20		8		11		1		8		9
wt%	av.	s.d.	av.	s.d.	av.	s.d.		av.	s.d.	av.	s.d.
SiO_2	71.43	0.43	69.88	1.97	72.24	0.51	71.23	72.14	0.35	71.29	0.36
TiO_2	0.04	0.02	0.03	0.03	0.04	0.02	0	0.04	0.04	0.03	0.02
Al_2O_3	14.74	0.17	14.63	0.32	14.02	0.16	14.27	14.41	0.15	14.68	0.18
FeO_t	0.61	0.14	0.65	0.07	0.63	0.12	0.49	0.64	0.05	0.69	0.11
MnO	0.08	0.07	0.09	0.04	0.05	0.04	0.09	0.11	0.11	0.1	0.09
MgO	0.03	0.01	0.05	0.02	0.06	0.03	0.06	0.06	0.03	0.05	0.02
CaO	0.31	0.04	0.33	0.06	0.36	0.02	0.3	0.38	0.04	0.22	0.04
Na_2O	3.6	0.12	3.57	0.13	3.57	0.2	3.82	3.37	0.19	4.14	0.33
K_2O	4.29	0.11	4.15	0.21	4.76	0.19	4.59	5.1	0.16	4.28	0.26
P_2O_5	0.46	0.13	0.35	0.06	0.29	0.13	0.39	0.24	0.09	0.43	0.08
ZnO	0.13	0.13	nd	nd	0.06	0.11	nd	0.05	0.09	0.11	0.12
F	0.6	0.07	1.16	0.51	0.25	0.09	1.12	0.25	0.03	0.2	0.1
Total	96.31	0.59	94.89	2.66	96.34	0.58	96.35	96.78	0.42	96.22	0.24

O=F	0.25	0.49	0.1	0.47	0.1	0.09
Total	96.06	94.40	96.24	95.88	96.68	96.14
A/CNK	1.32	1.33	1.2	1.21	1.22	1.24
A’	70.6	71.9	45.7	48.5	51.8	55.3
B’	9.7	10.5	10.8	8.2	10.9	11.3
Qz	35.4	35.1	34.2	32.7	33.8	32.1
Ab	32.2	32.6	31.8	34.3	29.9	37
Or	26.9	26.5	29.7	28.8	31.6	26.7
An	1.6	1.8	1.9	1.6	2	1.2
Co	3.8	4	2.5	2.6	2.8	3

MI: glass inclusion, n = number of analyses; av. = average; s.d. = standard deviation

All Fe as FeO

A/CNK = molar $Al_2O_3/(Na_2O+K_2O+CaO)$; A’ = 1000*(Al-(Na+K+2Ca)) atomic; B’ = 1000*(Fe+Mg+Ti) atomic

Qz, Ab, An, An, Co are normative concentrations of quartz, albite, orthoclase, anorthite and corundum

CR85-2		CR85-2		JV2		JV3		CH0	
matrix		MI		obsidian		obsidian		obsidian	
8		9		15		15		5	
av.	s.d.	av.	s.d.	av.	s.d.	av.	s.d.	av.	s.d.
71.44	0.46	70.05	0.98	72.24	0.48	70.24	0.47	69.91	0.48
0.01	0.02	0.00	0.03	0.04	0.03	0.03	0.03	0.03	0.03
14.69	0.31	14.66	0.17	15.79	0.22	16.51	0.2	16.36	0.25
0.58	0.12	0.85	0.37	0.57	0.13	0.4	0.11	0.39	0.09
0.07	0.07	0.18	0.09	0.05	0.07	0.08	0.08	0.06	0.05
0.04	0.02	0.04	0.02	0.01	0.01	0.01	0.01	0.02	0.02
0.21	0.03	0.24	0.05	0.22	0.03	0.16	0.03	0.17	0.03
3.89	0.26	3.01	0.30	4.11	0.14	4.37	0.08	4.62	0.13
4.68	0.21	5.18	0.36	3.69	0.07	3.65	0.07	5.14	0.04
0.43	0.11	0.47	0.08	0.56	0.11	0.67	0.19	0.55	0.1
0.1	0.13	nd	nd	0.05	0.11	0.06	0.09	0.1	0.17
0.21	0.1	0.43	0.19	1.33	0.09	1.89	0.09	1.81	0.14
96.35	0.91	95.11	0.81	98.67	0.67	98.07	0.68	99.17	0.99
0.09		0.18		0.56		0.8		0.76	
96.26		94.93		98.11		97.27		98.4	
1.24		1.33		1.41		1.44		1.22	
55.4		71.8		90.6		99.6		56.9	
9.08		12.8		8.7		6.3		6.4	
32.1		34.6		35.1		32.1		23.9	
34.7		27.4		36.2		38.9		40.6	
29.1		32.8		22.7		22.7		31.6	
1.1		1.3		1.2		0.9		0.9	

3	27.4	4.8	5.4	3	

Table 2. Trace element compositions of glass standards and obsidians

Sample	NIST610				BCR-2G					JV1		
Type	standard				control					obsidian		
n	35				10					2		
ppm	av. 1 σ	s.d.	RSD (%)	Ref*	av.	s.d.	RSD (%)	Ref**	Dv (%)	av.	s.d.	RSD (%)
		Ref***	Dv (%)									
Li	484.6	2.6	0.5	484.6	9.5	0.4	4.6	9.0	5.4	3354	24.3	0.7
	128.4	3440	-2.5									
Be	465.7	3.2	0.7	465.6	2.0	0.1	4.7	2.3	-12.8	38.5	0.6	1.6
	1.5	41.1	-6.4									
B	356.5	4.3	1.2	356.4	5.2	0.5	9.2	6.0	-13.2	1819	3.6	0.2
	71.9	1930	-5.8									
P	342.5	3.5	1.0	342.5	1243	15.9	1.3	1615	-23.0	1915	2.1	0.1
	131.1	2310	-17.1									
Ti	434.0	3.8	0.9	434.0	11293	119.2	1.1	14100	-19.9	206.0	2.8	1.4
	10.6											
Mn	433.3	1.7	0.4	433.3	1411	22.9	1.6	1550	-9.0	421.2	1.7	0.4
	15.7											
Zn	456.3	5.4	1.2	456.3	152.8	8.6	5.6	125.0	22.2	89.9	2.4	2.7
	4.5	94.5	-4.9									
Ge	426.3	2.8	0.7	426.3	1.7	0.1	8.6	1.5	10.0	4.6	0.2	4.7
	0.3											
Rb	431.1	2.4	0.6	431.1	48.9	1.3	2.6	47.0	4.0	1229	17.1	1.4
	48.8	1165	5.5									
Sr	497.5	3.3	0.7	497.4	301.7	14.4	4.8	342.0	-11.8	1.1	0.03	2.6
	0.1	1.6	-30.2									
Zr	440.0	2.9	0.7	439.9	160.2	9.1	5.7	184.0	-13.0	13.0	0.1	0.8
	0.6	39.0	-66.7									

Nb	419.41.9	1.644.0	0.41.0	419.4	9.9	0.4	3.8	12.5	-21.1	44.5	0.2	0.4
Sn	396.39.0	2.0175.0	0.5-7.1	396.3	1.8	0.0	2.2	2.6	-29.0	162.6	nd	nd
Cs	360.920.7	2.0541.0	0.52.5	360.9	1.1	0.0	3.4	1.2	-3.2	554.6	0.3	0.05
Ba	424.10.1	2.6<10	0.6	424.1	603.3	24.9	4.1	683.0	-11.7	1.1	0.1	7.2
La	457.50.04	3.61.6	0.8-45.8	457.4	23.8	1.4	5.9	24.7	-3.7	0.9	0.02	2.4
Sm	450.60.04	3.50.9	0.8-49.5	450.5	6.0	0.4	6.3	6.6	-9.1	0.4	0.04	9.6
Eu	461.20.003	3.80.02	0.8-59.3	461.1	1.8	0.1	5.7	2.0	-9.3	0.008	0.003	35.6
Gd	420.00.04	3.60.7	0.8-44.0	419.9	5.7	0.4	6.6	6.7	-15.0	0.4	0.1	22.5
Yb	461.70.03	4.30.4	0.9-31.8	461.5	3.1	0.2	6.5	3.4	-10.1	0.3	0.1	21.8
Ta	376.71.0	2.726.9	0.7-32.9	376.6	0.5	0.0	5.7	0.8	-31.3	18.1	0.3	1.8
W	445.43.2	2.964.7	0.715.5	445.3	0.5	0.1	14.5	0.5	7.3	74.7	0.3	0.4
Pb	413.40.3	2.87.0	0.77.7	413.3	10.2	0.5	4.9	11	-7.7	7.5	0.03	0.4
U	457.20.7	2.521.0	0.6-23.1	457.1	1.5	0.1	4.9	1.7	-11.7	16.1	0.1	0.7

n = number of analyses; av. = average; s.d. = standard deviation; RSD: relative standard deviation calculated as 100.(s.d./av.); 1 σ: average analytical error calculated with Glitter; Deviation (Dv) calculated as 100.(analysis-Reference)/Reference; nd: not determined

*Preferred average in Pearce et al. (1997)

**from the GeoRem database (Jochum et al., 2005)

***from Pichavant et al. (1987)

JV2						JV3				CH0		
obsidian/control						obsidian				obsidian/control		
59						9				45		
av.	s.d. 1 σ	RSD (%)	1 σ	Ref***	Dv (%)	av.	s.d.	RSD (%)	1 σ	av.	s.d.	RSD (%)
3310	186.0 69.9	5.6	122.4	3440	-3.8	4076	72.9	1.8	128.8	1522	73.2	4.8
38.6	3.8 6.2	9.8	2.3	41.3	-6.7	125.8	1.7	1.4	5.1	121.1	9.0	7.4
1775	61.2 128.4	3.4	88.8	1865	-4.7	2184	25.8	1.2	79.9	2199	116.0	5.3
1932.	140.9 260.5	7.3	202.5	2310	-16.4	2691	10.5	0.4	142.9	2218	441.1	19.9
217.7	27.6	12.7	18.8									
427.5	17.8 21.4	4.2	15.8							606.0	10.9	1.8
94.3	13.7 6.0	14.6	7.1	95.5	-1.3					89.2	9.9	11.1
4.7	1.4	29.4	3.5									
1190	30.9 64.0	2.6	43.3	1164	2.2	1431	13.4	0.9	47.7	1447	73.7	5.1
1.1	0.2 0.4	19.0	0.1	1.3	-15.2					3.1	0.7	21.5
13.3	1.3 0.5	9.9	0.7	34.0	-61.0					12.2	0.3	2.4
45.9	4.0 2.1	8.7	1.8	47.0	-2.4	44.9	0.3	0.6	1.7	44.4	2.8	6.3
184.3	9.8 12.3	5.3	7.4	202.5	-9.0	260.9	8.7	3.3	8.8	260.5	18.0	6.9
535.8	19.7 38.4	3.7	19.9	547.5	-2.1	795.4	14.8	1.9	37.8	829.5	49.5	6.0

1.1	0.4 0.9	33.3	0.3	<10					7.4	1.2	15.6
0.8	0.1 0.03	17.7	0.1	1.5	-41.9				0.6	0.02	2.3
0.4	0.1 0.01	28.3	0.1	0.5	-17.7				0.1	0.01	7.5
0.01	0.04 0.01	365.2	0.02	0.03	-64.5				0.01	0.002	19.7
0.5	0.2 0.02	53.3	0.2	0.6	-26.9				0.1	0.01	8.4
0.2	0.1 0.5	54.5	0.1	0.4	-38.2				0.2	0.01	4.9
18.6	2.4 1.6	12.8	0.9	26.7	-30.5	26.3	0.6	2.1	0.9	25.4	3.0	11.8
72.6	4.1 4.7	5.7	3.3	67.3	7.8	90.7	2.1	2.4	3.3	92.0	6.5	7.1
7.3	0.8 0.4	11.3	0.5	10.0	-27.4					8.6	0.3	4.0
15.7	1.3 0.8	8.1	0.7	26.0	-39.5	13.3	0.3	2.4	0.5	14.0	1.5	10.8

Table 3. Trace element compositions of matrix glasses

Sample	MH1				MA85-4				MA85-7			
Type	matrix				matrix				matrix			
n	13				10				10			
ppm	av.	s.d.	RSD (%)	1 σ	av.	s.d.	RSD (%)	1 σ	av.	s.d.	RSD (%)	1 σ
Li	687.2	128.8	18.7	25.5	115.1	18.6	16.2	5.0	126.1	21.2	16.8	8.0
Be	60.7	9.4	15.5	2.4	17.2	4.7	27.4	1.6	40.8	7.7	19.0	4.9
B	1367	103.5	7.6	54.9	799.0	37.4	4.7	41.5	837.3	85.7	10.2	53.4
P	1127	83.4	7.4	49.9	814.3	99.5	12.2	90.8	1047	289.9	27.7	657.8
Ti					282.5	22.4	7.9	19.6	271.0	16.0	5.9	35.5

Mn					289.2	20.1	6.9	11.4	397.1	30.0	7.6	16.5
Zn	67.4	17.4	25.9	3.5	58.1	15.2	26.2	6.2	94.3	39.8	42.3	27.3
Ge					6.6	2.1	31.6	2.9				14.3
Rb	883.4	40.8	4.6	30.0	694.4	52.5	7.6	24.4	686.0	60.6	8.8	28.0
Sr	19.1	5.7	30.0	0.8	13.9	1.5	11.1	0.7	18.6	8.1	43.6	1.5
Zr					13.1	1.5	11.7	0.7	14.8	2.3	15.5	1.4
Nb	24.0	2.7	11.4	0.9	22.2	1.5	6.5	1.1	23.9	1.9	8.0	1.4
Sn	35.2	7.7	21.7	1.5	61.7	5.9	9.6	3.0	53.1	8.8	16.6	4.1
Cs	313.0	20.9	6.7	9.9	162.4	19.6	12.1	7.3	170.0	25.4	15.0	6.5
Ba	33.7	10.8	32.1	1.7	21.2	2.8	13.2	1.7	20.7	7.8	37.8	3.1
La					1.66	0.33	20.1	0.16	1.55	0.25	15.9	0.3
Sm					0.36	0.15	41.9	0.16	0.54	0.35	65.1	0.4
Eu					0.05	0.03	57.1	0.03	0.11	0.06	56.7	0.1
Gd					0.15	0.11	69.7	0.13	0.31	0.16	51.8	0.3
Yb					0.28	0.17	61.4	0.13	0.28	0.17	61.2	0.3
Ta	8.8	1.4	15.6	0.4	4.9	0.9	17.8	0.29	6.2	1.2	19.7	0.7
W	41.4	5.0	12.0	1.9	19.4	3.4	17.7	1.2	24.2	4.9	20.4	2.5
Pb					18.4	3.5	19.0	1.0	18.4	3.3	17.8	2.3
U	14.7	1.7	11.2	0.6	16.5	3.2	19.2	0.7	17.4	2.7	15.7	1.3

n = number of analyses; av. = average; s.d. = standard deviation; RSD: relative standard deviation calculated as 100.(s.d./av.); 1 σ: average analytical error calculated with Glitter; nd: not determined

CR85-1 matrix 10				CR85-2 matrix 10			
av.	s.d.	RSD (%)	1 σ	av.	s.d.	RSD (%)	1 σ
544.5	76.3	14.0	18.6	489.2	80.6	16.5	18.1
96.7	2.4	2.5	3.1	96.0	2.6	2.7	3.1
1100	13.3	1.2	77.1	1089	18.9	1.7	97.8
1653	10.9	0.7	105.0	1689	19.4	1.1	111.2
125.7	2.0	1.6	4.2	124.3	3.0	2.4	4.3
492.6	13.3	2.7	17.0	531.2	20.7	3.9	19.9
81.9	4.2	5.2	2.9	82.9	5.1	6.1	3.2
4.2	0.2	4.5	0.2	4.0	0.1	3.7	0.2
858.6	6.2	0.7	32.5	888.8	11.1	1.3	38.1
5.9	0.2	3.7	0.2	5.2	0.7	12.9	0.2
10.9	0.1	1.2	0.4	10.8	0.1	1.2	0.4
20.8	0.2	0.9	0.7	20.9	0.2	1.1	0.8
82.3	1.6	2.0	2.8	81.9	2.7	3.3	3.0
287.9	5.9	2.1	10.8	286.6	5.5	1.9	12.1
10.5	0.9	8.9	0.4	10.8	1.7	16.1	0.4
0.79	0.02	1.9	0.03	0.76	0.01	1.2	0.04
0.15	0.02	13.2	0.01	0.16	0.02	10.5	0.01
0.03	0.003	10.8	0.003	0.02	0.005	19.1	0.003
0.15	0.01	6.9	0.01	0.17	0.01	8.0	0.01
0.26	0.01	4.1	0.02	0.26	0.02	7.0	0.02
8.6	0.1	1.6	0.3	8.3	0.1	1.4	0.4
25.2	0.6	2.2	0.9	25.4	0.4	1.4	1.1
13.5	0.4	3.2	0.5	13.4	0.9	6.9	0.5

13.9	0.3	2.0	0.5	13.5	0.2	1.5	0.6

Table 4. Trace element compositions of glass inclusions

Sample MH1												
MI#	m1 1 σ	m2	m3	m4	m5	m6	l1	j1	j2	av.*	s.d.*	RSD (%)
Host	Qz	Qz	Qz	Qz	Qz	Qz	Qz	Qz	Qz			
ppm												
Li	835.0 32.1	846.3	485.9	576.1	602.1	418.2	388.1	2312.1	2367.5	593.1	185.8	31.3
Be	60.8 4.2	52.2	60.9	52.3	53.8	54.5	36.8	26.1	21.9	53.0	8.1	15.2
B	1359 68.6	1384	1284	1242	1321	1319	1273	873.5	899.7	1312	49.7	3.8
P	n.d. 2.3	n.d.	n.d.	n.d.	n.d.	n.d.	n.d.	n.d.	n.d.	nd	nd	nd
Ti	264.7 28.3	220.2	264.5	231.7	218.1	198.9	230.6	306.4	341.8	232.7	24.3	10.5
Mn	392.4 15.3	392.6	378.7	399.5	441.2	351.9	320.2	322.0	333.8	382.4	38.2	10.0
Zn	92.9 7.9	106.1	78.8	86.2	87.6	77.9	54.2	104.3	104.6	83.4	16.0	19.2
Ge	<16.66 7.6	<16.68	<14.80	<16.09	<16.52	<20.97	<15.82	<15.85	<18.21	nd	nd	nd
Rb	871.8 42.5	900.6	897.7	891.1	888.4	893.4	910.4	830.7	1005.4	893.3	12.0	1.3

Sr	13.3 1.0	12.1	12.8	12.5	13.6	14.4	13.1	13.5	10.0	13.1	0.8	5.8
Zr	14.0 1.1	14.7	13.8	12.6	14.3	14.5	13.1	17.7	16.8	13.8	0.8	5.6
Nb	24.4 1.5	26.1	25.4	26.0	25.8	26.6	23.4	19.4	21.5	25.4	1.1	4.4
Sn	68.3 4.9	85.3	133.9	45.5	45.0	112.7	116.6	87.5	97.9	86.7	35.5	41.0
Cs	330.4 14.8	338.8	339.7	322.6	335.8	324.7	328.2	217.7	227.4	331.4	6.8	2.0
Ba	21.0 3.0	18.2	19.3	19.0	15.3	25.5	28.0	20.0	21.9	20.9	4.4	21.1
La	1.5 0.2	1.3	1.4	1.4	1.5	1.2	1.7	2.3	1.9	1.42	0.2	11.4
Sm	0.2 0.3	<0.00	<0.00	0.2	0.7	0.8	<0.00	1.6	0.5	0.46	0.3	75.6
Eu	<0.33 0.1	<0.228	<0.20	<0.36	<0.40	0.2	<0.43	<0.36	0.8	0.23	0.1	37.8
Gd	<0.74 0.4	<0.52	<0.65	<0.52	<0.74	<1.17	<1.03	<1.15	<1.02	nd	nd	nd
Yb	0.3 0.8	1.0	<0.00	0.2	<0.00	<0.00	<1.35	0.7	0.8	0.50	0.4	74.4
Ta	10.9 0.6	10.4	10.4	11.0	9.2	10.7	9.7	6.1	5.6	10.3	0.6	6.2
W	44.4 3.2	50.2	47.8	45.7	51.6	49.8	44.0	32.0	30.5	47.6	3.0	6.4
Pb	15.5 1.3	17.0	14.9	19.3	16.0	18.6	15.0	18.2	20.9	16.6	1.8	10.7
U	16.8 1.1	17.2	17.0	16.6	18.7	16.2	13.9	22.3	24.0	16.6	1.4	8.6

av. = average; s.d. = standard deviation; RSD: relative standard deviation calculated as 100.(s.d./av.); 1 σ: average analytical error calculated with Glitter; n.d. = not determined

*Calculated on the first seven compositions

CR85-2

b1	h1	h2	g1	av.	s.d.	RSD (%)	1 σ
Af	Qz	Qz	Qz				
254.8	192.0	210.7	347.5	251.2	69.4	27.6	19.6
112.1	32.5	40.1	95.9	70.1	39.8	56.7	6.0
1043	726.5	800.3	1016	896.4	156.9	17.5	61.7
n.d.	n.d.	n.d.	n.d.	n.d.	n.d.	n.d.	2.3
115.9	236.5	212.5	132.7	174.4	59.1	33.9	30.9
544.0	436.6	514.9	601.0	524.1	68.4	13.1	23.6
73.4	60.3	80.9	80.0	73.7	9.5	12.9	8.7
<24.93	<17.20	<20.33	<16.94	n.d.	n.d.	n.d.	9.2
936.7	805.9	970.9	907.2	905.1	71.1	7.9	53.9
5.9	5.3	7.0	3.5	5.4	1.5	27.3	0.7
13.0	11.0	10.3	11.2	11.4	1.1	10.0	1.2
21.1	23.4	29.6	23.5	24.4	3.6	14.9	1.7
87.0	69.7	88.4	102.0	86.8	13.2	15.2	6.0
353.8	277.8	364.8	326.3	330.7	38.8	11.7	18.1
5.6	6.6	15.9	8.0	9.0	4.7	51.8	2.5
0.6	1.0	1.0	1.1	0.92	0.2	21.8	0.2
<0.86	0.4	<0.00	<0.92	0.36	0.2	50.0	0.4
0.61	0.26	0.48	0.46	0.45	n.d.	n.d.	0.2
<1.76	1.3	1.8	0.4	1.15	0.8	72.0	0.6
0.2	0.3	0.2	0.3	0.26	0.0	17.4	0.7
7.7	6.3	8.7	9.2	8.0	1.3	15.8	0.6
28.7	17.5	29.2	25.8	25.3	5.4	21.4	2.5
13.9	14.8	16.9	16.1	15.4	1.3	8.7	1.5

19.1	13.3	15.8	14.6	15.7	2.5	15.8	1.2	

Table 5. Mineral/melt partition coefficients

	Qz/L Ilm/L		Pl/L		Af/L		Biot/L		Mu/L		And/L	
El.	K_d K_d	error error (%) (%)	K_d	error (%)	K_d	error (%)	K_d	error (%)	K_d	error (%)	K_d	error (%)
Li	0.21 0.85	20 21	0.45	20	0.13	20	3.66	20	1.12	20	0.01	25
Be	0.007 0.02	23 53	0.10	19	0.03	33	0.06	20	0.10	7	0.01	32
B	0.001	22	0.003	19	0.002	25	0.004	12	0.04	5	0.003	16
Al	0.005	7										
P	0.005	43	0.61	11	0.81	15	0.06	11	0.07	8	0.13	11
Ti	0.14	9	0.14	8	0.10	11	92.8	6	19.8	6		
Mn	0.001 21.9	22 11	0.087	9	0.02	11	4.12	8	0.32	7		
Zn	0.011 21.5	46 30	0.032	45	0.03	42	18.8	29	1.61	10	0.14	31
Ge	0.20 0.14	28 122	0.51	16	0.44	41	0.81	10	0.61	12		
Rb	0.0002 0.0001	21 62	0.008	7	0.98	10	2.87	8	1.75	5	0.005	
Sr	0.002 0.06	51 51	10.8	33	8.87	26	0.11	33	0.30	17	0.007	53

Zr	0.0004 1.39	51 19	0.003	24	0.0003	72	0.14	16	0.21	5		
Nb	0.0001 91.2	64 12	0.003	37	0.0003	46	9.75	11	4.30	5	0.01	31
Sn	0.002 0.22	33 25	0.048	21	0.18	18	0.44	20	0.53	7	0.07	28
Cs	0.001 0.0005	21 49	0.0007	20	0.03	14	0.46	10	0.08	5	0.002	23
Ba	0.001 0.28	75 47	0.87	35	33.0	29	5.02	35	3.30	20	0.01	59
La	0.001 0.01	74 82	3.57	7	0.34	21	0.005	37	0.002	51		
Sm	0.012	132	0.68	30	0.02	142	0.01	113	0.01	111		
Eu	0.018	138	17.9	25	16.8	62	0.11	71	0.29	46		
Gd	0.018 0.26	170 123	0.45	31	0.05	121	0.02	79	0.03	78		
Yb	0.038	100	0.02	107			0.03	85	0.05	45		
Ta	0.0001 43.2	59 23	0.004	48	0.0005	72	2.35	19	0.63	5	0.005	47
W	0.0002 0.44	68 28	0.003	28	0.001	79	0.38	15	2.10	6	0.0021	50
Pb	0.003 1.18	48 25	2.98	12	5.68	22	0.24	11	0.23	9		
U	0.0001 0.04	75 25	0.008	21	0.003	35	0.01	17	0.01	12	0.0002	83

K_d are median values calculated with matrix glasses as described in text. See Table S4 for details of the calculations

Errors are relative errors (median values) calculated with equation (1)

Table 6. Mass fractions of phenocrysts in Macusani magmas and bulk partition coefficients used in the modelling

Mass fractions

phenocryst	Qz	Pl	Af	Biot	Mu	Ilm	And	total
case a	0.330	0.239	0.367	0.051	0.006	0.000	0.007	1.000
case b	0.375	0.136	0.417	0.058	0.007	0.000	0.007	1.000
case c	0.404	0.293	0.225	0.063	0.007	0.000	0.008	1.000
case d	0.339	0.246	0.377	0.026	0.006	0.000	0.007	1.000
case e	0.417	0.303	0.232	0.033	0.007	0.000	0.008	1.000
case f	0.473	0.172	0.263	0.074	0.008	0.000	0.009	1.000

Bulk partition coefficients (D)

element	Li	B	Rb	Sr	Nb	Sn	Cs	Ba	Ta	W	Pb
case a	0.42	0.002	0.52	5.84	0.53	0.10	0.03	12.60	0.13	0.03	2.81
case b	0.42	0.002	0.59	5.17	0.60	0.11	0.04	14.19	0.14	0.04	2.79
case c	0.49	0.002	0.42	5.17	0.65	0.09	0.04	8.01	0.15	0.04	2.17
case d	0.33	0.002	0.46	6.00	0.28	0.10	0.02	12.80	0.07	0.02	2.88
case e	0.38	0.002	0.34	5.33	0.35	0.08	0.02	8.11	0.08	0.03	2.23
case f	0.49	0.002	0.49	4.20	0.76	0.09	0.04	9.24	0.18	0.05	2.03

For each element, $D = \Sigma\ x.K_d$ where x is the mass fraction of a given phenocryst, K_d is from Table 5 and the summation is on all phenocrysts of the assemblage

case a: reference case, mass fractions of phenocrysts calculated from average modal compositions of ash-flow tuffs (Pichavant et al., 1988a)

case b: vol% Pl lowered by 50% in comparison with a

case c: vol% Af lowered by 50% in comparison with a

case d: vol% Biot lowered by 50% in comparison with a

case e: vol% Af and Biot both lowered by 50% in comparison with a

case f: vol% Pl and Af both lowered by 50% in comparison with a

Table 7. Results of trace element modelling

Element	$C_{matrix\ glass/MIs}$ C minimum (JV1/JV2)	C maximum (JV3)	C_0 f (%) (JV1/JV2)	C_0 f (%) (JV3)	Model best fit	C_L (JV1/JV2)	C_L (JV3)
B	799.0 2183.1	1366.5 1798.0	799.0 2183.1 44	799.0 37	FC, all cases	1798.0	
Rb	686.0 1337.2	918.0 1209.5	686.0 1430.8 43	686.0 33	FC, case e	1172.4	
Sr	11.8 1.1	19.1	19.1 41	19.1	FC, case f	1.4	0.77
Nb	20.4 45.2	25.4 44.9	20.4 33	20.4 33	FC, case d	36.4	42.0
Sn	57.4 173.4	92.7 260.9	80* 43	103* 37	FC, case e	168.6	261.0
Cs	162.4 545.2	331.4 795.4	250* 42	302* 35	FC, case a	544.8	797.0
Ba	20.7 1.1	33.7	33.7 45	33.7	FC, case c**	1.1	0.47
Ta	4.9 18.3	10.3 26.3	8.8* 46	10.3* 37	FC, case d	18.7	26.3
W	19.4 73.7	47.6 90.7	32* 42	34* 37	FC, case a	69.8	89.8
Pb	16.6 7.4	19.5	19.5 44	19.5	FC, case c	7.6	6.0

Concentrations (C) in ppm.

$C_{matrix\ glass/MIs}$: minimum and maximum trace element concentrations in matrix glasses and MIs (Tables 3 and 4)

C_0: concentration in liquid parental to either JV1/JV2 or JV3, taken as the minimum $C_{matrix\ glass/MIs}$ except when otherwise noted (*), see text

FC: fractional crystallization (equation (3)). Cases a-f refer to the mass fractions and D in Table 6

C_L: concentration in final liquid (i.e., calculated for $C_L(B)=C(B)$) where C(B) refers to either JV1/JV2 or JV3

C: concentration in obsidian, either JV1/JV2 or JV3 (Table 2). For JV1 and JV2 averages are given

f: fraction of residual liquid calculated with equation (5)

**FC calculation performed with adjusted D value, see text